Advances in Nano Research, *Vol. 12, No. 5 (2022) 529-547*
https://doi.org/10.12989/anr.2022.12.5.529

High-velocity ballistics of twisted bilayer graphene under stochastic disorder

K. K. Gupta[1], T. Mukhopadhyay*[2], L. Roy[1] and S. Dey[1]

[1]*Department of Mechanical Engineering, National Institute of Technology Silchar, Silchar, India*
[2]*Department of Aerospace Engineering, Indian Institute of Technology Kanpur, Kanpur, India*

(*Received September 20, 2021, Revised November 11, 2021, Accepted March 18, 2022*)

Abstract. Graphene is one of the strongest, stiffest, and lightest nanoscale materials known to date, making it a potentially viable and attractive candidate for developing lightweight structural composites to prevent high-velocity ballistic impact, as commonly encountered in defense and space sectors. In-plane twist in bilayer graphene has recently revealed unprecedented electronic properties like superconductivity, which has now started attracting the attention for other multi-physical properties of such twisted structures. For example, the latest studies show that twisting can enhance the strength and stiffness of graphene by many folds, which in turn creates a strong rationale for their prospective exploitation in high-velocity impact. The present article investigates the ballistic performance of twisted bilayer graphene (tBLG) nanostructures. We have employed molecular dynamics (MD) simulations, augmented further by coupling gaussian process-based machine learning, for the nanoscale characterization of various tBLG structures with varying relative rotation angle (*RRA*). Spherical diamond impactors (with a diameter of 25Å) are enforced with high initial velocity (V_i) in the range of 1 km/s to 6.5 km/s to observe the ballistic performance of tBLG nanostructures. The specific penetration energy (E_p^*) of the impacted nanostructures and residual velocity (V_r) of the impactor are considered as the quantities of interest, wherein the effect of stochastic system parameters is computationally captured based on an efficient Gaussian process regression (GPR) based Monte Carlo simulation approach. A data-driven sensitivity analysis is carried out to quantify the relative importance of different critical system parameters. As an integral part of this study, we have deterministically investigated the resonant behaviour of graphene nanostructures, wherein the high-velocity impact is used as the initial actuation mechanism. The comprehensive dynamic investigation of bilayer graphene under the ballistic impact, as presented in this paper including the effect of twisting and random disorder for their prospective exploitation, would lead to the development of improved impact-resistant lightweight materials.

Keywords: ballistic performance; coupled molecular dynamics simulation; Gaussian process regression; Monte Carlo simulation; twisted bilayer graphene

1. Introduction

Graphene has been a center of attraction for the last few decades to the research community owing to its versatile capabilities in numerous domains (Song *et al.* 2016, Adhikari and Chowdhury 2012, Fazelzadeh and Ghavanloo 2014, Kashyap *et al.* 2020, Sharma *et al.* 2021, Cui *et al.* 2016, Wong *et al.* 2019). Ever since graphene is physically realized (Geim and Novoselov 2010) and experimentally characterized (Lee *et al.* 2008), it has been explored extensively to harness its extraordinary mechanical characteristics of mechanical strength, stiffness and low density along with other unprecedented multi-physical features that have proven its worth in materializing novel classes of composites (Stankovich *et al.* 2006, Kwon *et al.* 2017, Li *et al.* 2018, Shingare *et al.* 2019, Chandra *et al.* 2022, Nasker *et al.* 2022). High-velocity impact is the physical phenomenon that is often encountered during space exploration and military combat. The exceptional intrinsic strength and stiffness with low mass density make graphene a potential candidate for the development of ballistic protection materials. In this regard, Avila *et al.* (2011) reported an increase in ballistic impact resistance with the addition of graphene nanoparticles in the hybrid nanocomposites. Similarly, O'Masta *et al.* (2017) investigated the impact resistance of multilayer graphene (MLG) and polyvinyl alcohol (PVA) based composite and observed that the ballistic limit of the composite was 50% higher than the aluminium films. In 2014, Lee *et al.* (2014) carried out a miniature projectile impact test on the multilayer graphene (MLG) sheets with a thickness in the range of 10 to 100 nanometers. They observed that the specific penetration energy (E_p^*) of MLG is 10 times higher than the macroscopic steel at the projectile velocity of 600 meters per second. These experimental findings have drawn the attention of the research community to explore the behaviour of graphene further subjected to high-velocity impact.

Molecular dynamics (MD) simulation is one of the most economical and feasible options to characterize nanoscale materials (Gupta *et al.* 2020, Roy *et al.* 2021, Shahini *et al.* 2021, Lin *et al.* 2017, Sunnardianto *et al.* 2021, Farazin and Mohammadimehr 2020, Sha'bani and Rash-Ahmadi 2021). The MD simulations of nanoscale high-velocity impact tests have been in practice in the research community for a wide range of materials for the last few years, a few of these studies revealed the understanding of failure mechanism, stress wave propagation, and perforation behaviour of nanoscale materials subjected to high-velocity ballistic

*Corresponding author, Professor,
E-mail: tanmoy@iitk.ac.in

ISSN: 2287-237X (Print), 2287-2388 (Online)

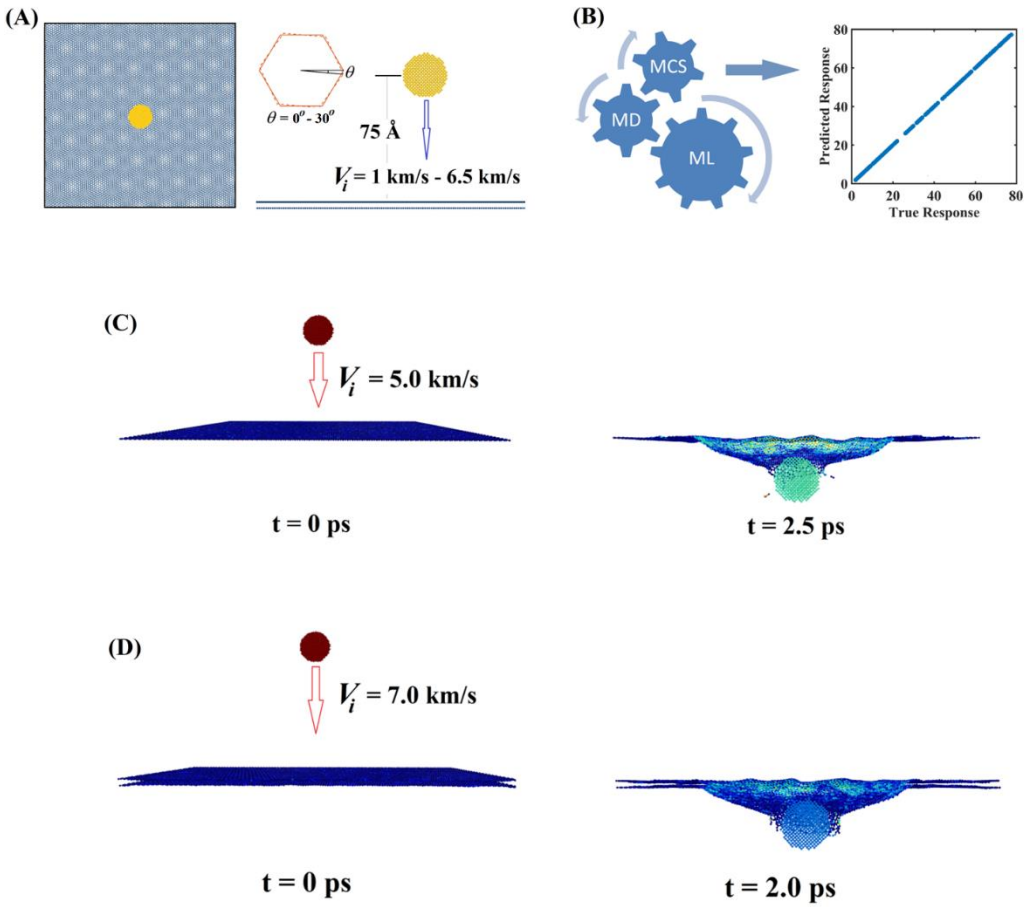

Fig. 1 Ballistics of twisted bilayer graphene; (A) Representation of relative rotation angle *(RRA)* and impact velocity in the stipulated range for performing MD simulation of impact analysis (B) Integration of MCS, MD simulations and ML algorithm to deduce the deep data-driven computational insights for the ballistic performance of tBLG structures (C) Complete penetration of SLGS (200 Å x 200 Å) at the initial impact velocity of 5 km/s (D) Complete penetration of AA stacked BLG (200 Å x 200 Å) at the initial impact velocity of 7 km/s. The post-impact alteration in the colour of the impactor indicates the variation in its velocity.

impact (Dewapriya and Miller 2021, Noori *et al.* 2021, Dewapriya and Meguid 2019, Bizao *et al.* 2018, Hosseini-Hashemi *et al.* 2018, Azevedo *et al.* 2018, Xia *et al.* 2016, Haque *et al.* 2016). Likewise, Yoon *et al.* (2016) investigated the specific penetration energy (E_p^*) of perfect and defected graphene sheets by penetrating graphene with silica and nickel nanoparticles. Tian *et al.* (2019) performed the finite element and MD based nano impact test on the hexagonal boron nitride (hBN) sheets and deduced that the impact strength of hBN is superior to the conventional armour materials.

The bilayer/multilayer graphene nanostructure has also been found to be a superior material to absorb the high kinetic energy (O'Masta *et al.* 2017, Haque *et al.* 2016). The effective mechanical properties of graphene-based multilayer heterostructures are found to become programmable as the number of layers increases (Mukhopadhyay *et al.* 2017a, b). It has been reported by Zheng *et al.* (2019) that the intrinsic strength and stiffness of bilayer graphene (BLG) can be enhanced by twisting the top layer with respect to the bottom layer in some relative rotation angle (*RRA*). Mukhopadhyay *et al.* (2020) proposed a prospective modulation capability of elastic modulus for twisted bilayer van der Waals heterostructures corresponding to the variations in twist angle. To this end, a few groups investigated the sustainability of twisted bilayer graphene (tBLG) structures against hypervelocity impact by nano-projectiles. For instance, Peng *et al.* (2021) twisted the top layer of BLG with nine different angles in the range of 0° to 30° and carried out the high-velocity impact test on the tBLG structures. They concluded that the tBLG structures were able to withstand higher impact velocities in comparison to AA (*RRA* = 0°) stacked BLG. Similarly, Qiu *et al.* (2020) carried out the series of atomistic simulations of nano impact test on tBLG structures comprising six different cases of twisting angles (within 0° to 30°) and deduced that the rebound velocity of projectile decreases as the twisting angles of tBLG structure increases. A much more detailed investigation on the high-velocity impact of twisted bilayer structures with the increased instances of twisting angles was carried out by Yang and Zhang (2021), wherein they investigated the tBLG and twisted graphene-hBN bilayer structures.

The brief literature review presented in the preceding paragraphs summarizes the most recent studies performed to characterize the ballistic response of twisted bilayer

structures. It is noteworthy to mention that the studies so far carried out are restricted to few discrete values of twisting angles and the impact velocities. To have complete insight into the material behaviour it is essential to gather the responses for large-scale unknown sample points within the occurrence bounds of the considered parameters (Gupta *et al.* 2021, 2022a, b, Mukhopadhyay *et al.* 2016, Mahata *et al.* 2016, Yin *et al.* 2021, Trinh and Mukhopadhyay 2021). For addressing this issue, in the present study, we would integrate the MD simulation approach with Monte Carlo sampling (MCS) and Gaussian process machine learning (ML). In the first stage, the MCS based samples of control parameters associated with the study (relative rotation angle (*RRA*) and initial velocity of impactor (V_i)) would be (algorithmically-) generated within the stipulated range of variation. A series of MD simulations would be performed for the generated samples, providing the sample space for training, testing and validation of the GPR based ML model. The generalization capability of the ML model would further be assessed on the basis of percentage error between the original and predicted responses. The present study aims to focus on the ballistic performance of considered tBLG structures in terms of specific penetration energy (E_p^*) and post-impact residual velocity of the impactor (V_r). The effect of random disorder in the influencing sources would be accounted for by carrying out Monte Carlo simulations involving multiple stochastic system parameters. Carrying out direct MCS based MD simulations is an exorbitant task considering the computational expense associated with each of the MD simulations. The powerful generalization capability of the ML-based model would be utilized to predict the responses for a large number of samples (~10^4) for this purpose, based on which the intricate ballistics of tBLG structures would be revealed that otherwise would have remained unexplored. Thus the novel scientific contribution of this paper can be perceived in capturing and prospective exploitation of the complete continuous domain of twisting angles along with the effect of random system disorder for the ballistic performances of tBLG structures by integrating a data-driven ML approach with conventional MD simulations (refer to Fig. 1). Hereafter, the paper is organized as: section 2 provides all necessary details for the coupled simulation, section 3 presents detailed numerical results and discussion, and finally concluding remarks are provided in section 4.

2. Modelling and simulation

The accuracy and ingenuity of the results obtained from the MD simulations greatly depend on the adopted interatomic potential. In the present study, we have utilized the AIREBO-Morse force field to model the graphene sheets, wherein the Lennard-Jones potential in the conventional AIREBO force field is replaced with Morse potential to correctly mimic the high-pressure deformation and breaking of bonds (Shoaib *et al.* 2021, Haque *et al.* 2016). The AIREBO-Morse potential can be mathematically represented as

Table 1 Range of variation in the control variables associated with the present study

Control variables	Range of variation
Relative rotation angle (*RRA*)	0°–30°
Velocity of impactor (V_i)	1 km/s – 7 km/s

$$E_{AIREBO-M} = \frac{1}{2}\sum_{i}\sum_{j\neq 1}(E_{ij}^{REBO} + E_{ij}^{MORSE} + \sum_{k\neq i,j}\sum_{l\neq i,j,k} E_{ij}^{TORSION}) \quad (1)$$

where

E_{ij}^{REBO} = REBO term

E_{ij}^{MORSE} = Morse term

$E_{ij}^{TORSION}$ = Torsional energy term

and the morse term can be represented as

$$U_{ij}(r) = -\varepsilon_{ij}\left[1-\left(1-e^{-\alpha_{ij}(r-r_{ij}^{eq})}\right)^2\right] \quad (2)$$

The parameters ε and r_{eq} denote minimum energy terms (depth and location) and α denotes the modified curvature of the potential energy with the minimum separation (O'Connor *et al.* 2015). The interlayer distance between the two layers of graphene is kept at 3.4 Å, and the separation is modelled with the Lennard-Jones potential with energy parameter as 0.00239 eV and distance parameter as 2.5 Å (Zhang *et al.* 2021). The spherical diamond impactor in the present study is modelled with Tersoff (Tersoff 1988) force field as it is the best-suited potential to model C-C interaction in the diamond. The distance between the considered graphene structures (SLGS and BLG) and the centre of the spherical diamond impactor is maintained as 75 Å in every case. The interaction between graphene structure and spherical diamond impactor is modelled with the morse force field.

The MD simulations are performed in LAMMPS (Plimpton 1995) environment and the dumped trajectories are visualized in OVITO (Stukowski 2009). The graphene structures are primarily generated through VMD (Humphrey *et al.* 1996), which are later customized as per the twisting angle in MATLAB (2018). The clockwise rotation of the top layer is carried out as

$$[X_i, Y_i, 1]_{rotated} = [X_i, Y_i, 1]\begin{bmatrix}1 & 0 & 0\\ 0 & 1 & 0\\ -Tx & -Ty & 1\end{bmatrix}\begin{bmatrix}\cos\theta & -\sin\theta & 0\\ \sin\theta & \cos\theta & 0\\ 0 & 0 & 1\end{bmatrix}\begin{bmatrix}1 & 0 & 0\\ 0 & 1 & 0\\ Tx & Ty & 1\end{bmatrix} \quad (3)$$

where X_i and Y_i are the x and y coordinates of the top layer, T_x and T_y are the mid coordinates of the top layer and θ corresponds to the twisting angle. The control variables considered in the present study and their corresponding range of variation are presented in Table 1.

A dataset with algorithmically generated 128 samples is constructed first within the stipulated range of variation for the two system parameters mentioned in Table 1. Further, MD simulations of nanoscale impact are carried out for each of these instances. To perform the simulations, all four edges of the considered graphene structures are clamped up to the width of 5Å by setting the force and velocity

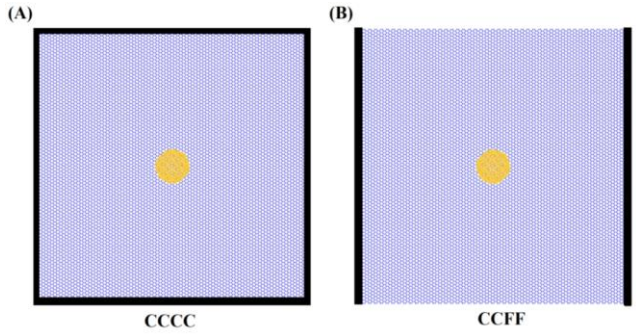

Fig. 2 The boundary conditions adopted in the impact-induced free vibration study. (A) CCCC denotes that all edges are clamped (B) CCFF denotes that two opposite edges are clamped and the other two edges are kept free

components to zero. An iteration time step of 0.5 femtoseconds (fs) is adopted for the MD simulation. Prior to running the nanoscale impact simulations, the potential energy of the structure is minimized with the conjugate gradient method. The minimization is performed for 25 ps. Further, the structure is thermalized at room temperature (≈ 300 K) using a Berendsen thermostat for the next 25 ps. Once the structure is relaxed at room temperature, the structure is impacted with a rigid spherical diamond impactor under an NVE ensemble. The impact simulations are carried out for another 20 ps. To derive the ballistic responses, the variation in the kinetic energy and the post-impact residual velocity of the spherical impactor are observed.

2.1 Specific penetration energy (E_p^*) and post-impact residual velocity of the impactor (V_f)

Specific penetration energy may be defined as the kinetic energy of the impactor dissipated by the material subjected to the high-velocity impact with respect to the unit mass of the material in the impact zone. The mathematical formulation of E_p^* may be represented as (Dewapriya and Miller 2021)

$$E_p^* = \frac{KE_i - KE_r}{M} \tag{4}$$

where KE_i and KE_r denote the initial and residual kinetic energy of the impactor, respectively. The values of KE_i and KE_r are estimated by observing time-history of the kinetic energy of the impactor, as shown in figure S1(B) of the *Appendix*. The term M in the denominator denotes the mass of the impactor zone. The mass of the impactor zone is determined by the following equation

$$M = \pi.R^2.N_l.\rho_A \tag{5}$$

where R denotes the radius of the impactor zone (same as impactor), N_l denotes the number of layers, and ρ_A denotes the area density of graphene, which is taken as $0.77\text{x}10^{-6}$ kg/m^2 (Haque *et al.* 2016) in the present study.

The residual velocity of the impactor is determined by observing the post-impact trajectory of the spherical impactor (as presented in Fig. S1(A) of the *Appendix*). The negative sign of residual velocity indicates the rebound of the impactor, whereas the positive sign indicates a complete penetration. Hence, the sign of residual velocity is only considered to indicate the direction of post-impact movement of the impactor.

2.2 Impact-induced resonant behaviour of graphene structures

It is observed that the ballistic impact of diamond impactor induces a free vibration phenomenon in the considered graphene nanostructures. So far, a vast amount of studies have been carried out to deduce the resonant behaviour of graphene (Tian *et al.* 2017, Kwon *et al.* 2013, Kang *et al.* 2013). However, these studies used different mechanisms of excitation. In the present study, we have carried out a deterministic analysis taking length (200Å-600Å, with constant width 200Å in all cases), V_i (1 km/s-4 km/s), and boundary conditions (CCCC-CCFF) as the control parameters, wherein we have excited the considered nanostructures with high-velocity impact of the spherical diamond impactor (with diameter 25 Å). The boundary conditions adopted in the analysis corresponding to resonant behaviour of graphene structures are illustrated in figure 2. It can be noted here that all the ballistic impact performances are measured by enforcing CCCC boundary conditions alone while the resonant frequency of the structures is deduced using both the above-mentioned boundary conditions for the sake of more clarity. The free vibration simulations are performed with the same initial conditions as used for impact simulations. However, after running the impact simulation for 15ps, the spherical diamond impactor is removed and the free vibration of graphene nanostructures is performed with NVE ensemble for 500 ps. During the free vibration of graphene nanostructures, the time-history of variation in kinetic energy of the structure is captured and the time-domain signal is converted to the frequency domain by performing its fast Fourier transform (as shown in Fig. S2(A-B) of *Appendix*). Subsequently, the resonant frequencies are estimated corresponding to the peaks of the amplitudes.

2.3 GPR based ML model

The dataset for training, testing and validation of the ML model is constructed by employing an algorithm-driven sampling technique, wherein a uniform distribution of samples is followed within each parametric range for the required number of samples (128 in the current case). The mathematical formulation of sampling can be represented as follows

$$\varphi_i = \varphi_{\min} + r_i\,(\varphi_{\max} - \varphi_{\min}) \tag{6}$$

where ($\varphi_{max} - \varphi_{min}$) stands for the range of variation of the control parameter, φ_{min} represents the minimum value of the control parameter, and r_i denotes the random number drawn from the probabilistic distribution in the range of 0 to 1. The variable φ_i provides the i^{th} realization of the sampled parameter, where $i \in (1{:}N)$, N denotes the total number of samples considered.

Table 2 Comparison of the E_p^* reported in the literature and obtained in the present investigation. (N_l = no. of layers, D_i = Diameter of impactor, V_i = impact velocity in m/s, E_p = penetration energy, E_p^* = specific penetration energy)

Literature	N_l	D_i	V_i (m/s)	E_p (eV)	E_p^* (MJ/kg)
Lee *et al.* (2014) Exp.	127-154	3.7 μm	600, 900	-	1.09, 1.26
Bizao *et al.* (2018) MD	1	140 Å	900	-	15
Yoon *et al.* (2016) MD	1	48 Å	5000	-	42
Xia *et al.* (2016) MD	1	50 Å	2000	1745	-
Xia *et al.*(2016) MD	1	68 Å	2000	4156	-
Haque *et al.*(2016)MD	1	12.1 Å	5000	-	40.8
Haque *et al.*(2016)MD	2	12.1 Å	5000	-	25.2
Replication of Xia *et al.*(2016)	1	50 Å	2000	1986.49	-
Replication of Xia *et al.*(2016)	1	68 Å	2000	4197.51	-
Replication of Haque *et al.*(2016)	1	12.1 Å	5000	-	49.9
Replication of Haque *et al.*(2016)	2	12.1 Å	5000	-	23.6
Present study (MD)	1	25 Å	2000	-	12.85
Present study (MD)	1	25 Å	5000	-	75.07
Present study (MD)	2	25 Å	2000	-	7.25
Present study (MD)	2	25 Å	5000	-	45.15

The responses are collected by performing the MD simulation corresponding to 128 samples. The resulted dataset is further utilized to train and test the GPR based ML model. To enforce simultaneous training-testing and prevent over-fitting, the 5-fold cross-validation algorithm is used. The 5-fold cross-validation scheme splits the dataset into five sets, wherein at a time only four sets are used for training the model and the remaining one set is used for testing. The GPR based model is trained by using *'Matern52'* as the kernel function and *'quasinewton'* optimization to optimize the training process. The '*Random'* active set method is employed for regression by enforcing *'Exact'* fit and predict method. The goodness of fit of the model is assessed by correlation coefficient (R^2 value), while the predictive accuracy of the model is assessed on the basis of percentage error in the responses derived from direct MD simulation and the ML prediction corresponding to unseen random testing datasets (Gupta *et al.* 2021, Burn and Popelier 2020, Deringer *et al.* 2021). A detailed description of GPR based model along with its mathematical formulation is provided in section A2 of the *Appendix*.

3. Results and discussion

Validation of the findings obtained from the MD simulations is an integral part of nanoscale characterization. In this regard, we have carried out a few sets of simulations to validate the derived values of E_p^*. The findings of the validation are reported in Table 2, wherein an excellent agreement between the current results and literature can be observed. With the adequate confidence established by such validation studies, we would further dive in-depth to comprehensively assess the high-velocity ballistic performance of graphene structures considering different critical parametric influences. In the following subsections, we have reported the ballistic and impact-induced resonant behaviour of single-layer graphene sheet (SLGS), bilayer graphene (BLG), and twisted bilayer graphene (tBLG) structures.

3.1 Ballistic performance of SLGS

In this analysis, a square-shaped SLGS with the size of 200 Å x 200 Å is impacted with a spherical diamond impactor having a diameter of 25Å. The distance between centre of the spherical impactor and SLGS is kept 75Å. The initial velocity of the impactor is varied from 1km/s to 7km/s at the interval of 0.5km/s. The findings of the high-velocity impact on the SLGS are illustrated in figure 3 (also refer to figure S3, for further visualization). The residual velocity of the spherical impactor corresponding to different impact velocities is plotted in figure 3(A). The negative sign of residual velocity corresponds to the rebound stage, while the positive residual velocity denotes the complete penetration of SLGS. It is noteworthy from figure 3(A) that the complete penetration of SLGS occurs at the impact velocity of 5 km/s, supporting the observation made by Yoon *et al.* (2016). It also clearly depicts that the limiting velocity for the SLGS impacted with the spherical diamond impactor of diameter 25 Å lies in between the transitional regime of 4.5 km/s and 5 km/s. The E_p^* value of each case is reported in Fig. 3(B), wherein it is evident that E_p^* increases as the impact velocity increases. The peak appears at 5 km/s; beyond the impact velocity of 5 km/s, stagnation in the rise of specific penetration energy of SLGS is recorded. To explore the complete penetration of SLGS subjected with high velocity (beyond 5 km/s) impact, the time-history of lateral displacement of SLGS is observed

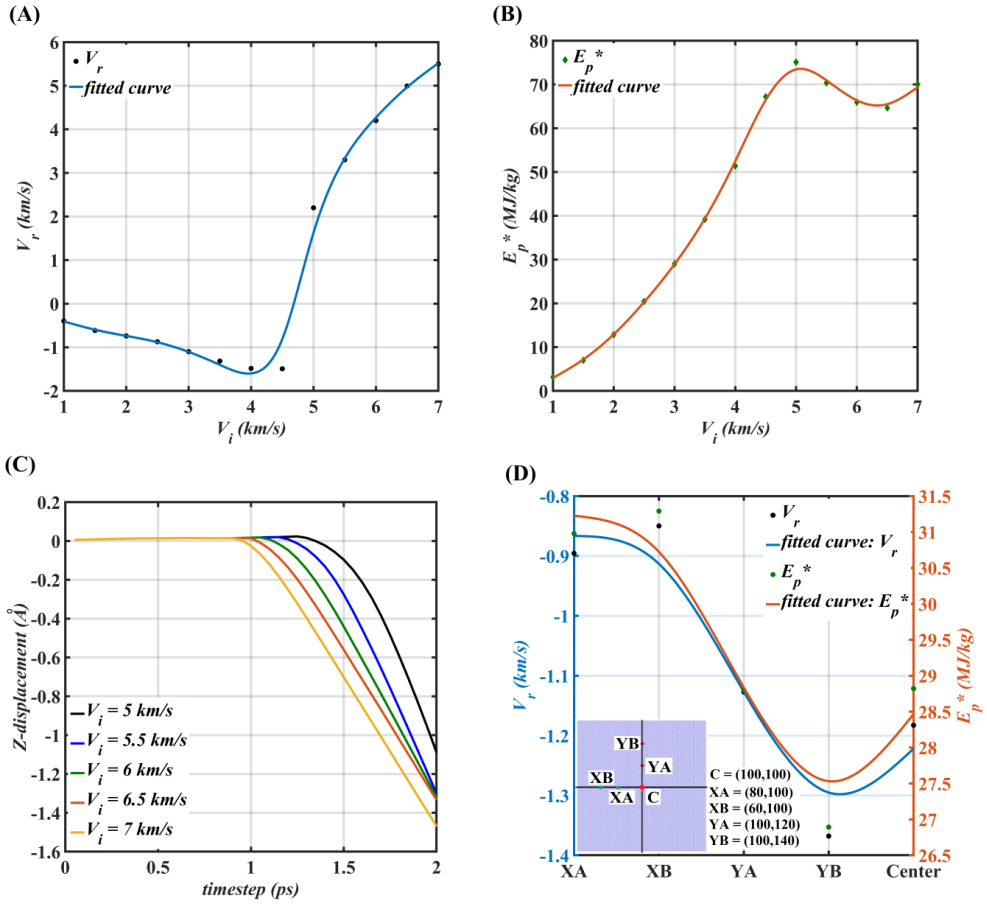

Fig. 3 Ballistic performance of SLGS. (A) Variation in residual velocity of the impactor with respect to the increase in initial impact velocity (B) Variation in specific penetration energy of SLGS with respect to the increase in initial impact velocity (C) Time history of complete penetration of SLGS subjected with the impact velocity in the range of 5 km/s – 7 km/s (D) Variation in V_r and E_p^* of SLGS corresponding to the location of impact (The X-axis presents different locations, as shown in the inset)

(refer to Fig. 3(C)). The sudden drop of the curve depicted in Fig. 3(C) denotes the complete penetration of SLGS. It is evident from the plot that as the impact velocity increases beyond 5 km/s, the time of complete penetration shifts toward the left, indicating an early failure of SLGS subjected to increment in impact velocity from 5 km/s to 7 km/s.

In the preceding analysis, the rigid diamond impactor is impacted at the centre of SLGS (X = 100 Å, Y = 100 Å) in all the cases. To assess the influence of location of impact on the ballistic performance of graphene structure, four different impact locations (XA = (80,100), XB = (60,100), YA = (100,80), and YB = (100,60)) are selected (the four locations used are depicted pictorially in the inset of Fig. 3(D)). These four locations are impacted with the impact velocity of 3 km/s with the rigid spherical diamond impactor. The variations in the residual velocity of the impactor and specific penetration energy of SLGS corresponding to the location of impact are presented in Fig. 3(D). It is evident from the observation that the impact at the locations XA and XB results in lower V_r values of the impactor and higher E_p^* values of SLGS, when compared with the cases of impact at the centre, YA and YB locations. This can be explained by the observations made by Haque *et al.* (2016), wherein they reported lower stress wave velocity at the impact points towards X direction when compared with the impact points towards the Y direction. The higher stress wave velocity generated in the material by high-velocity impact contributes to a higher rebound velocity of the impactor.

In the previous studies, the complete penetration of SLGS at relatively lower impact velocities (≈ 1km/s to 2 km/s) has been reported (Bizao *et al.* 2018, Haque *et al.* 2016). To address this discrepancy, we carried out a few simulations with gradually increasing the diameter of the impactor. The SLGS with the size of 500Å x 500Å is adopted in this study with a decreased timestep of 0.1 femtoseconds and the diameter of the impactor is increased gradually from 25Å to 150Å (25, 50, 75, 100, and 150 Å). The distance between the spherical impactors and the SLGS is maintained same as in the earlier simulations. The timestep is decreased in the present set of simulations to accurately deduce the findings as the number of atoms is elevated in this analysis (Dewapriya and Miller 2021). The initial velocity of the impactor is kept at 2 km/s for each instance. The findings drawn from the impactor size-dependent analysis are illustrated in Fig. 4. It is evident from Fig. 4(A), that as the diameter of the impactor is

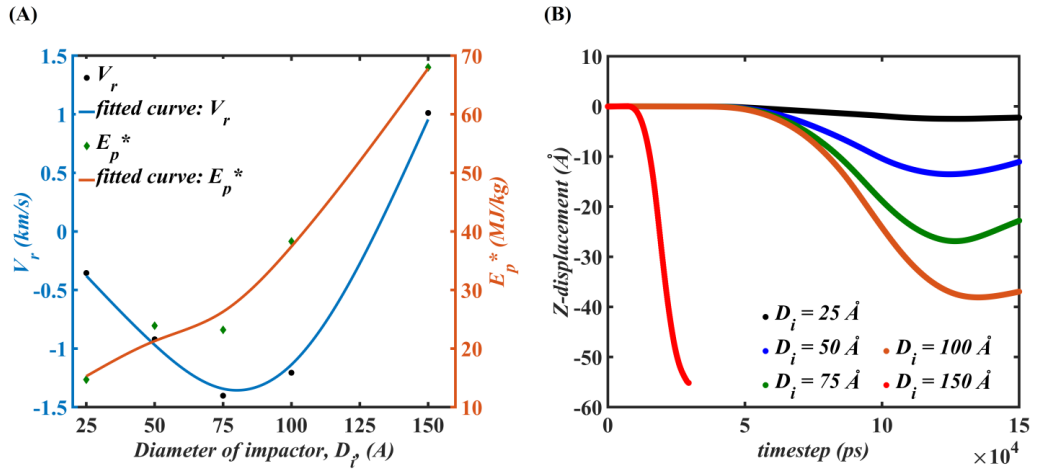

Fig. 4 Influence of impactor size on the ballistic performance of SLGS. (A) Variation in residual velocity and specific penetration energy corresponding to the increase in the diameter of the spherical diamond impactor (B) Lateral displacement of graphene sheet with respect to the increase in diameter of the spherical diamond impactor

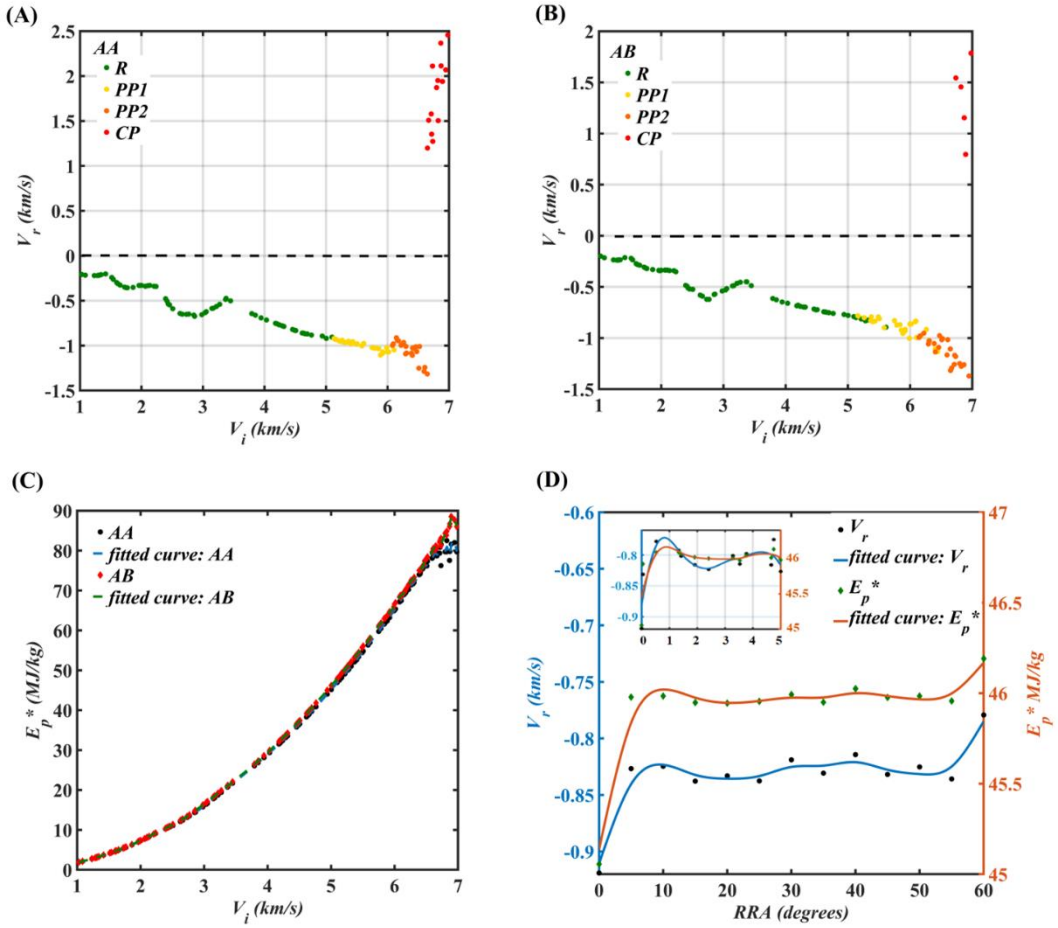

Fig. 5 Ballistic performance of AA and AB stacked BLG. (A) Variation in residual velocity of the impactor with the increase in impact velocity for the AA stacked graphene (B) Variation in residual velocity of the impactor with the increase in impact velocity for the AB stacked graphene. The green scatter points indicating the *'R'* stage denote the rebound of the impactor without any damage to the BLG structures. The yellow and orange scatter points indicating the *'PP*1*'* and *'PP*2*'* stages denote the partial penetration and rebound of the impactor with damage in the top layer and both layers, respectively. The complete penetration is denoted by the *'CP'* stage, indicated by red scatter points. (C) Variation in specific penetration energy of AA and AB stacked BLG (D) Variation in residual velocity of the impactor and specific penetration energy of tBLG structures with the increase in RRA. 0° stands for the AA stacked BLG and 60° stands for the AB stacked BLG

increased to 150 Å, the complete penetration was achieved at the velocity of 2 km/s 3 (also refer to Fig. S4, for further visualization). For the cases of diameter below 150 Å, the residual velocities of the impactor are rebound in nature. It can also be observed from Fig. 4(A), that the size of the impactor has a positive effect on the E_p^* values of SLGS. Fig. 4(B) illustrates the out-of-plane transverse displacement of the SLGS impacted with different sizes of the impactor. It is worth noting that the depth of impact cone of SLGS increases as the size of the impactor is increased and a sharp dive in the curve can be noticed with the case of complete penetration. The analysis depicted in Fig. 3(C-D) and Fig. 4 are restricted here to the SLGS structure and it is expected that the bilayer graphene structures would follow the same trend.

3.2 Ballistic performance of BLGs

In this subsection, two different stackings (AA (0°*RRA*) and AB (60°*RRA*)) of BLG are considered, each with the size of 200Å x 200Å. To limit the computational expense, the impactor with a diameter of 25Å is utilized and the initial position of the impactor is maintained at the same height as in the previous simulations. The initial impact velocity (V_i) is varied in the range of 1 km/s to 7 km/s. The quasi-random dataset (with the variation in impact velocity) with 128 samples is constructed for each case of stacking to prepare a sample space of 256 samples in total. In the next stage, the MD simulations are carried out for the constructed 256 instances. The findings of these MD simulations are illustrated in Fig. 5.

Figs. 5(A) and 5(B) presents the scattered data of the residual velocities for AA and AB stacked BLG, respectively with the variation in initial impact velocity. The distinctive colour patterns of scatter points represent different stages of post-impact scenarios. The impact velocity domain covered by green scatter points depicts the rebound stage without any damage to the BLG structure *'R'* and the corresponding residual velocity of the impactor. Likewise, the impact velocity domains covered by yellow and orange scatter points denote two different partial penetration stages *'PP*1*'* and *'PP*2*'*, wherein *PP*1 represents the partial penetration and rebound of the impactor with damage limited to the top layer of BLG and *PP*2 represents the partial penetration and rebound of the impactor with damage to both layers of BLG. The red scatter points represent the *'CP'* stage which denotes the complete penetration of BLG structures. It is evident from the figure that for both the cases of stacking the transition from *PP*2 to *CP* stage occurs in between the impact velocity of 6.5 km/s to 7 km/s. However, the AB stacked BLG depicts less occurrence of *CP* stage when compared with AA stacked BLG, indicating the enhanced impact resistance of twisted bilayer graphene sheets. From Fig. 5(C) it may be concluded that for both the stacking cases the values of E_p^* increase with the increase in velocity. It is worth mentioning that up to the impact velocity of 6.5 km/s the plots almost overlap each other; however, beyond the 6.5 km/s (in the *CP* stage) the scatter in the plots is more visible and the former rise in the E_p^* values comes to an asymptotic condition (similar to the SLGS). Another conclusion that is drawn to this end is that the ballistic performance of AA and AB stacked graphene almost matches with each other, but AB stacked BLG shows more strength against the *CP* stage in comparison to AA stacked BLG. This leads to a strong rationale for exploring the ballistic performance of BLGs subjected to the rotated top layer in more detail. In this regard, the top layer of the BLG structure is rotated with respect to the bottom layer in the range of 0° (AA) to 60° (AB) in the interval of 5°. The tBLG nanostructures are impacted by spherical diamond impactor with an initial impact velocity of 5 km/s. The ballistic performance of tBLG structures is reported in Fig. 5(D), and it is evident from the findings that the twisted BLG structures depict higher specific penetration energy and lower residual velocity of the impactor, when compared with the AA stacked BLG. The variation pattern displays a sharp rise in the ballistic performance of tBLG structures within the *RRA* of 0° to 5°, followed by almost constant ballistic performance measures in between the span of 5° to 55° *RRA*, and the ballistic measures are again slightly increased at 60° (AB). The sharp rise in the ballistic performance observed within the twist angle of 0°-5° is further explored deterministically to capture the accurate variation trend of residual velocity and specific penetration energy of tBLG structures (refer to the inset provided in Fig. 5(D). The plots reveal that even the slightly twisted BLG structures result in better ballistic performances, when compared with AA stacked BLG. This concludes that the twisted structures dissipate the maximum kinetic energy of high-velocity impactor when compared with AA stacked graphene structures. It can be explained by an increase in intrinsic mechanical properties and increased kinetic energy dissipation of the tBLG structures (Zheng *et al.* 2019, Peng *et al.* 2021). To explore the deep insights of ballistic performance of tBLG structures a separate MCS based sample space with 128 instances is fed to the GPR based ML model, considering *RRA* as another control variable along with V_i, which is presented in the later stage of subsection 3.4.

3.3 Impact induced resonant behaviour of graphene nanostructures

In this subsection, we have first validated the resonant behaviour of single-layer graphene nanoribbon (GNR) with the results published in previous literature. Moving ahead, we have utilized the excitation mechanism of high-velocity impact to deduce the resonant behaviour of graphene structures considered in the present study. The complete methodology to estimate the resonant frequency of the nanostructures is elaborated in subsection 2.2. The findings of the validation of resonant frequency are presented here in Table 3. With this understanding, a parametric analysis is carried out for resonant frequencies of the considered nanostructures, wherein, the resonant frequencies are assessed as a function of the increase in length (200Å-600Å, while width maintained as constant at 200 Å), initial impact velocity (1 km/s – 4 km/s), and the boundary conditions (CCCC - CCFF). The impact velocity is limited to 4 km/s in the present analysis to avoid the permanent deformation (/damage) of the structure. The observations of

Table 3 Validation of resonant frequency with available literature

Literature	Size of GNR	Excitation	Resonant frequency, R_f (GHz)
Tian *et al.*(2017)	300Å x 40Å	1.77nN transverse force at each atom	99.7
Kwon *et al.*(2013)	140Å x 7Å	9.5 nN transverse force at each atom	80
Kang *et al.*(2013)	141Å x 7Å	0.00608 nN – 6.08 nN transverse force at each atom	20 – 190
Replication of Tian *et al.* (2017) (for validation)	300Å x 40Å	1.77nN transverse force at each atom	80
Present study	300Å x 200Å	Transverse high-velocity impact of 30 Å/ps (3 km/s)	96

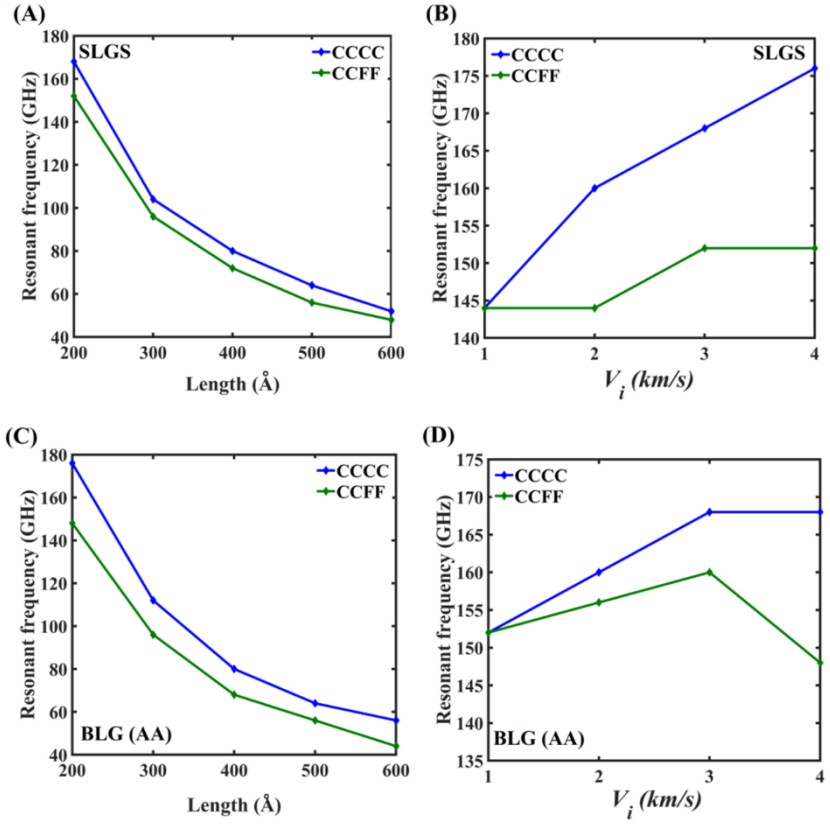

Fig. 6 Impact induced resonant behaviour in graphene nanostructures. (A) The resonant frequency (R_f) of SLGS as a function of length and enforced boundary conditions (B) The resonant frequency (R_f) of SLGS as a function of initial impact velocity and enforced boundary conditions (C) The resonant frequency (R_f) of AA stacked BLG as a function of length and enforced boundary conditions (D) The resonant frequency (R_f) of AA stacked BLG as a function of initial impact velocity and enforced boundary conditions

free vibration of SLGS and BLG (AA stacked) structures are presented in Fig. 6. It is evident from the figure that the CCCC boundary condition results in slightly higher resonant frequencies (R_f) due to higher global stiffness, regardless of SLGS or BLG structure. This is also observed that the BLG structures result in higher resonant frequencies when compared with the SLGS structures.

The increase in length has the inverse effect on the R_f values for both SLGS and BLG nanostructures, regardless of boundary conditions, which can be supported by the observations presented in Chandra *et al.* (2020). With the increase in initial impact velocity, the R_f values show slight variation, albeit without any particular trend. We further assessed the influence of *RRA* on the resonant frequencies (refer to the Fig. S2(C) of the *Appendix*); however, no major change in the corresponding R_f values is noted.

3.4 Integrated GPR based ML model for characterizing random system disorder and stochasticity

In this subsection, the results obtained from the integration of MD simulations and GPR based ML model, leading to large-scale data-driven insights, are interpreted. In the first part of the study illustrated in this subsection, the analysis is limited to two different stacking conditions, AA (*RRA* = 0°) and AB (*RRA* = 60°), wherein the impact

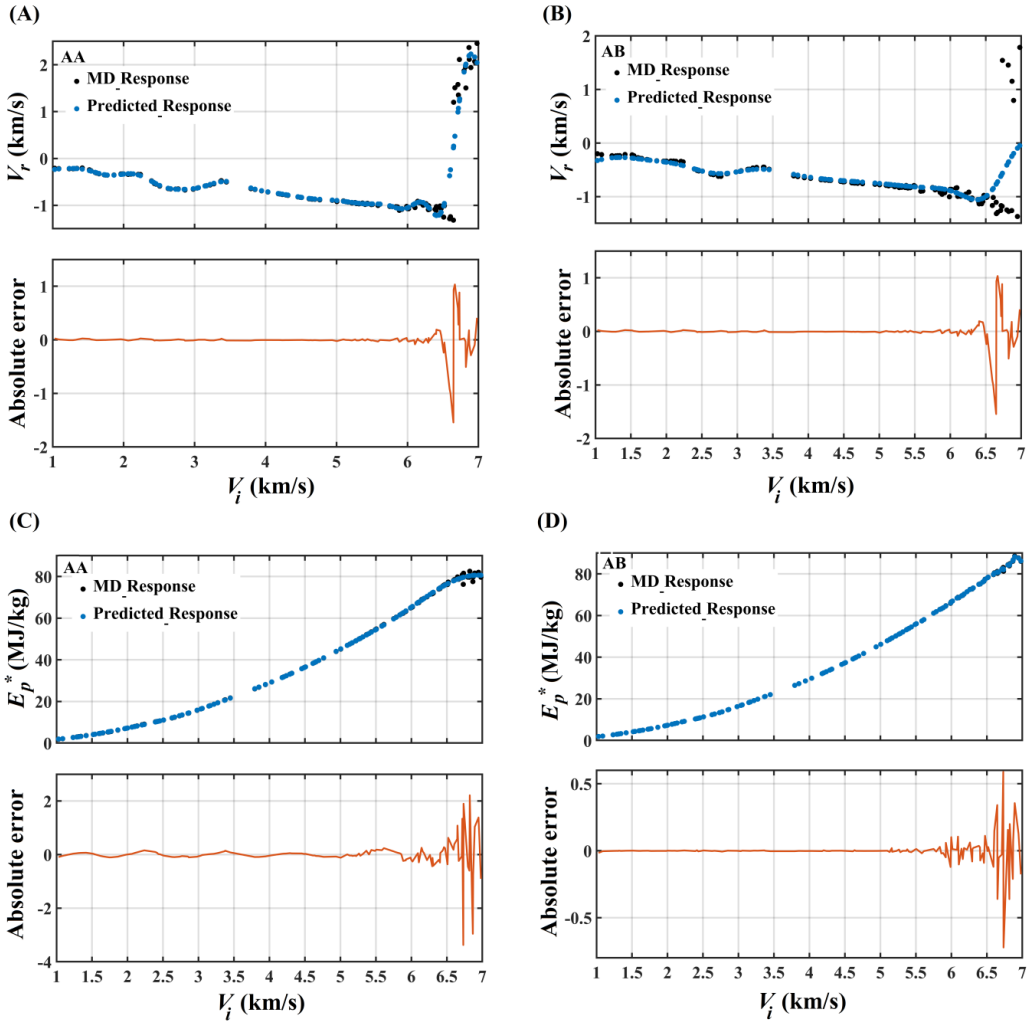

Fig. 7 Primal screening of GPR based ML model for AA and AB stacked BLG. (A) The variation trend and error profile of residual velocity for AA stacked BLG (B) The variation trend and error profile of the residual velocity for AB stacked BLG (C) The variation trend and error profile of the specific penetration energy for AA stacked BLG (D) The variation trend and error profile of the specific penetration energy for AB stacked BLG.

velocity is considered as the only input parameter. For the comprehensive characterization of the influence of impact velocity on the ballistic responses of AA and AB stacked BLG, the GPR based ML model is constructed. The primal screening to validate the GPR based model is presented in Fig. 7. Figs. 7(A) and 7(B) illustrates the error profile of predicted residual velocities for the cases of AA and AB stacked BLG, separately. Likewise, Figs. 7(C) and 7(D) reports the error profile of predicted specific penetration energy for the cases of AA and AB stacked BLG. It is evident from Fig. 7 that for both the ballistic responses, the ML model is able to comply with the acceptable error up to the *PP*2 stage only. The sudden transition of the process from *PP*2 to *CP* stage beyond the impact velocity of 6.5 km/s, makes it difficult for the GPR based ML model to generalize the responses due to completely different physics involved at the two stages. Hence, further in the following ML-based analysis, we limited the impact velocities within the range of 1.0 km/s - 6.5 km/s to construct the models. Moreover, the objective of the present study is limited to fully characterizing the ballistic performance of graphene nanostructures prior to the *CP* stage. Hence, out of 256 samples 218 samples (leaving the samples having velocities more than 6.5 km/s) are used to construct the GPR based ML model for in-depth assessment. The validation and error analysis of the GPR based ML model for the ballistic impact performance of AA and AB stacked BLG is presented in Fig. 8. By the assessment drawn through scatter plots and probabilistic error profiles depicted in Fig. 8, it is clear that the model is computationally efficient to predict both the ballistic performance features (V_r and E_p^*) with significant level of accuracy. Hence, the model is further deployed to determine the residual velocities and specific penetration energies under random disorder due to stochasticity in system parameters based on a full-scale MCS.

The findings drawn from the prediction of MCS for both the cases of stacking (AA and AB) are reported in Fig. 9. Figs. 9(A) and 9(C) illustrate the occurrence bound and probabilistic distribution of residual velocities and specific penetration energies for the AA and AB stacked BLG (within the impact velocity range of 1.0 km/s - 6.5 km/s).

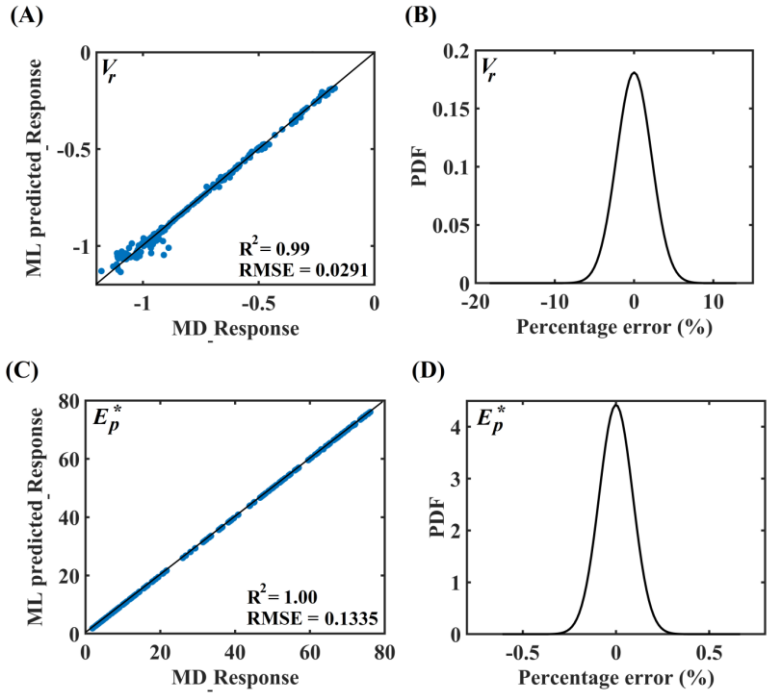

Fig. 8 Validation of GPR based ML model for AA and AB stacked BLG. (A) Scatter plot between the MD derived residual velocity and ML predicted residual velocity (B) Probability density function plot for the percentage error of predicted residual velocity (C) Scatter plot between the MD derived specific penetration energy and ML predicted specific penetration energy (D) Probability density function plot for the percentage error of predicted specific penetration energy

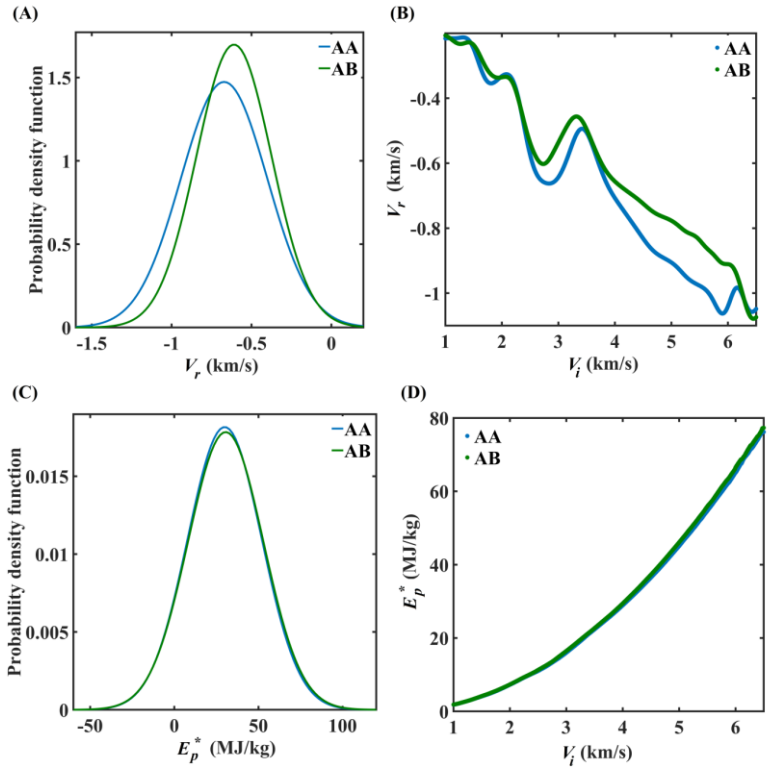

Fig. 9 Predicted large-scale data-driven ballistic responses obtained based on MCS concerning AA and AB stacked BLG. (A) Statistical distribution of residual velocity corresponding to AA and AB stacked BLG with respect to stochastic impact velocity (B) Variation trend of residual velocity corresponding to AA and AB stacked BLG captured by GPR based ML model (C) Statistical distribution of specific penetration energy corresponding to AA and AB stacked BLG with respect to stochastic impact velocity (D) Variation trend of specific penetration energy corresponding to AA and AB stacked BLG captured by GPR based ML model.

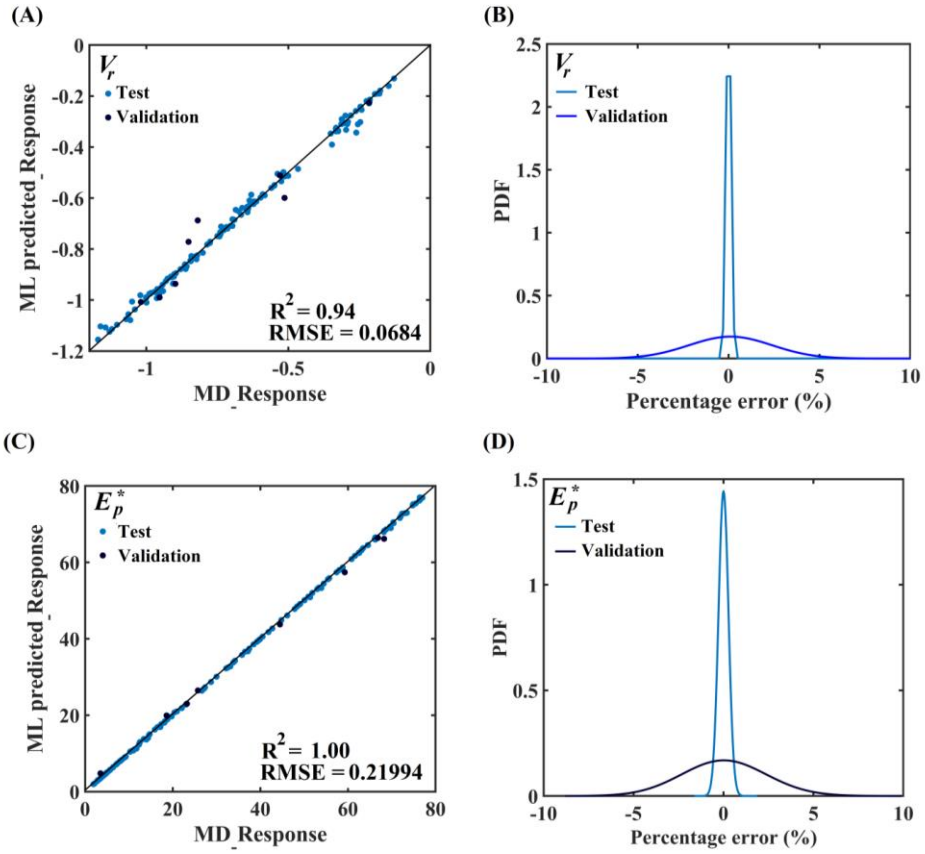

Fig. 10 Validation of GPR based ML model for tBLG structures. (A) Scatter plot between the MD derived residual velocity and ML predicted residual velocity (B) Probability density function plot for the percentage error of predicted residual velocity (C) Scatter plot between the MD derived specific penetration energy and ML predicted specific penetration energy (D) Probability density function plot for the percentage error of predicted specific penetration energy

Figs. 9(B) and 9(D) depict the variation profile of predicted residual velocities and specific penetration energies (for both AA and AB stacked BLG). It is noteworthy to observe that the stochastic variation profiles depicted in figure 9(B, D) exactly match with the deterministic profiles provided in figure 5(A-C), which indicates the computational prediction of the proposed GPR based ML model.

Once the computational efficiency of the GPR based ML model is established, we included the *RRA* as another variable along with initial impact velocity (V_i). Note that it is often extremely difficult to prepare nano-scale samples with the exactly designed *RRA*, leading to inevitable stochastic system disorder. Thus it is critically important to quantify the effect of such random structural disorders coupled with other system parameters. At this stage, a sample space with 128 instances is algorithmically constructed comprising of two control variables *RRA* and V_i (with a range of variation, *RRA*: 0° to 30° and V_i: 1 km/s to 6.5 km/s). The range of *RRA* is limited from 0° to 30° due to the symmetry in observations perceived by the deterministic findings reported in Fig. 5(D). The training and testing datasets were developed by conducting MD simulations for these 128 samples, and 8 samples, separately derived from a random distribution with the same parametric range as mentioned above. The validation of the ML model is illustrated in Fig. 10, which demonstrates a satisfactory generalization capability of the GPR based ML model for both the ballistic responses (V_r and E_p^*). With sufficient confidence in the constructed model, the model is further deployed to reveal deep computational insights on the ballistic performances of tBLG structures within the *RRA* ranging from 0° to 30° and V_i ranging from 1 km/s to 6.5 km/s. The large-scale data-driven characterization is carried out with the help of the proposed ML model by employing MCS with 10000 algorithmically generated random sets of input parameters.

The findings concerning the ML-based prediction of V_r and E_p^* are reported in Figs. 11 and 12, respectively. Figure 11(A-C) presents the occurrence bounds and probabilistic variation of residual velocities of the impactor with the individual variation in *RRA* and V_i and also corresponding to the compound variation of *RRA* and V_i. Figs. 11(D) and 11(E) reports the variation profiles of V_r against the *RRA* and V_i, which follow the same trend depicted by deterministic variation illustrated in Figs. 5(D) and 5(A), respectively. It can be concluded from the findings that the *RRA* has relatively less influence on the V_r compared to V_i, which is also established by the data-driven sensitivity analysis provided further in Fig. 11(F). Similar conclusions as above can be drawn in terms of stochastic evaluation of E_p^* reported in Fig. 12. The stochastic variation in impact velocity has a more prominent effect on the E_p^* when

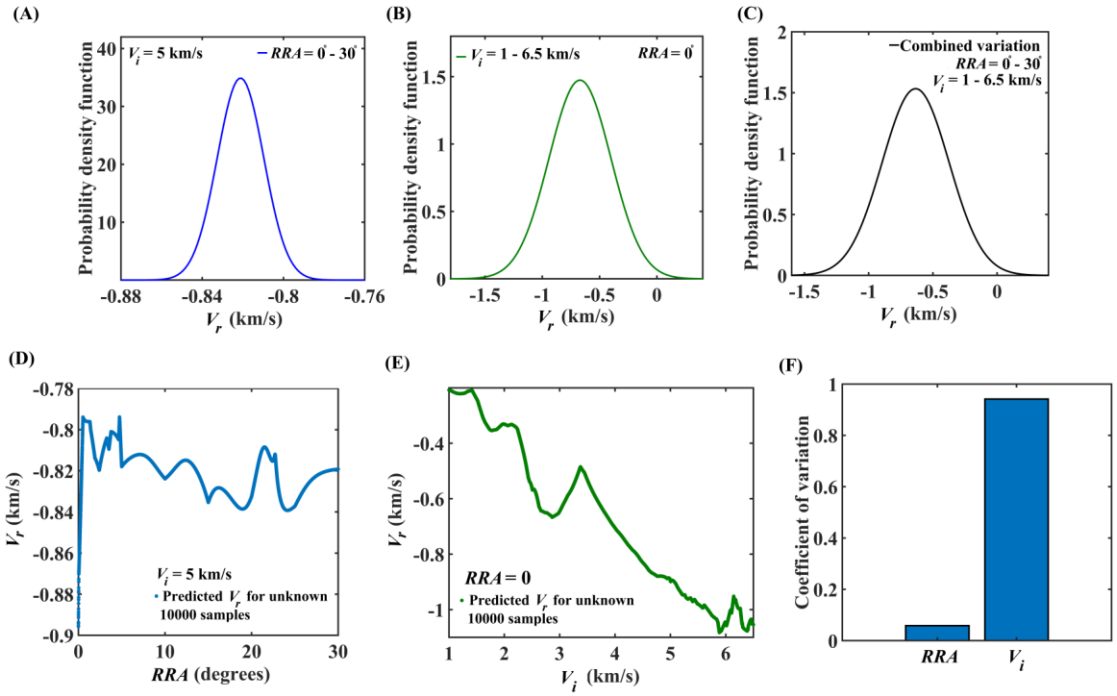

Fig. 11 MCS based predicted post-impact residual velocity of impactor for tBLG structures. (A) Statistical distribution of residual velocity corresponding to variation in *RRA* with a constant impact velocity of 5 km/s (B) Statistical distribution of residual velocity corresponding to variation in impact velocity with constant *RRA* at 0° (C) Statistical distribution of residual velocity corresponding to variation in both *RRA* and impact velocity of impactor (D) Variation trend of residual velocity with respect to increasing *RRA*, captured by ML model (E) Variation trend of residual velocity with respect to increasing impact velocity of the impactor, captured by ML model (F) Variance based sensitivity analysis for the residual velocity of impactor.

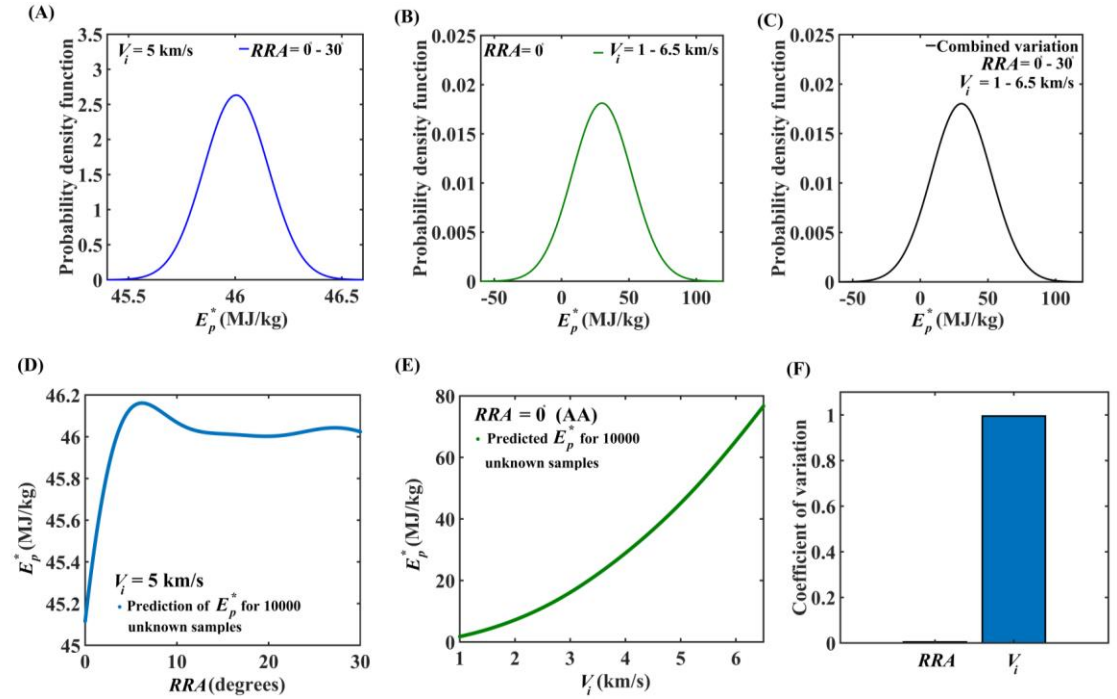

Fig. 12 MCS based predicted specific penetration energy for tBLG structures. (A) Statistical distribution of specific penetration energy corresponding to variation in *RRA* with a constant impact velocity of 5 km/s (B) Statistical distribution of specific penetration energy corresponding to variation in impact velocity with constant *RRA* at 0° (C) Statistical distribution of specific penetration energy corresponding to variation in both *RRA* and impact velocity of impactor (D) Variation trend of specific penetration energy with respect to increasing *RRA*, captured by ML model (E) Variation trend of specific penetration energy with respect to an increasing impact velocity of impactor, captured by ML model (F) Variance based sensitivity analysis of specific penetration energy.

compared with the variation in *RRA* (as evident from Figs. 12(A), 12(B), 12(F)). The stochastic variation profile of E_p^* presented in Figs. 12(D) and 12(E) affirms the trend of deterministic variation reported in Fig. 5(C) and 5(D). However, it is evident that the machine learning-based models are able to efficiently capture the intricate details of coupling multiple system parameters including the effect of random system disorder following a large-scale data-driven probabilistic framework. Interestingly, the numerical results reveal that even a small degree of stochasticity in the form of random disorder in twist angle can result in significantly enhanced specific energy absorption capacity, which leads to the realization of prospective exploitation of such inevitable random disorders.

4. Conclusions

This article investigates the capability of bilayer twisted graphene nanostructures subjected to high-velocity ballistic impact under the influence of intrinsic stochastic disorder. The residual velocity (V_r) of the impactor and specific penetration energy (E_p^*) are considered as the performance measures, wherein the influence of multiple critical structural and impactor parameters have been probed including their compound effects. In this regard, we have employed spherical diamond impactor to demonstrate hypervelocity ballistic impact throughout the present study.

A comprehensive investigation is presented here under high-velocity impact, starting from preliminary MD simulations considering SLGS, wherein we observe that the spherical diamond impactor having the diameter of 25Å, completely penetrates SLGS (of size 200Å x 200Å) at the initial impact velocity of 5 km/s. For the considered impact velocities below 5 km/s, the spherical impactor shows a rebound behaviour without damaging the SLGS. To assess the influence of the size of the impactor on the ballistic performance of SLGS (of size 500Å x500Å), we have gradually increased the diameter of the spherical diamond impactor from 25Å to 150Å (25, 50, 75, 100, and 150Å). It is observed that the impactor with a diameter of 150Å completely penetrates SLGS at a relatively lower impact velocity (≈ 2 km/s) when compared with the impactor having a diameter of 25 Å. We have proceeded further with the spherical diamond impactor of 25Å diameter to investigate BLG structures of size 200Å x 200Å. At this stage, we have also reported the free vibration behaviour of SLGS and BLG as a derivative of high-velocity impact analysis, wherein we demonstrate the parametric influence of an increase in the size, impact velocity and adopted boundary conditions on the resonant frequencies. It is revealed from the analysis that the CCCC boundary condition results in increased resonant frequency when compared with the results associated with CCFF boundary conditions, regardless of the SLGS or BLG configurations. An increase in the length of the structure, with width kept constant, is found to have an inverse influence on the resonant frequencies. These observations are found to be consistent for both SLGS and BLG configurations. The study further reveals that *RRA* has no major influence on the resonant behaviour of BLG structures. However, it is evident from the observations that BLG structures possess higher resonance frequencies compared to SLGS.

In the next stage, we have explored the ballistic performance of two differently stacked (AA and AB) BLG configurations subjected to initial impact velocity ranging from 1 km/s to 7 km/s. Total 128 random samples are generated for each case of stacking (AA and AB), with impact velocity as the randomly varying input parameter, resulting in 256 MD simulations to determine the residual velocity and specific penetration energy for each instance. The findings of these simulations conclude that both AA and AB stacked BLG are able to sustain the high-velocity impact up to 5 km/s without damage in any of the layers. The values of V_r and E_p^* increase with the increasing impact velocity up to the partial penetration with rebound stage. Another conclusion that is drawn to this end is that the ballistic performance of AA and AB stacked graphene almost matches with each other, but AB stacked BLG shows more strength against complete penetration compared to AA stacked BLG.

In general, the primary deterministic findings derived from the ballistic impact of tBLG structures reveal that the tBLG structures dissipate more kinetic energy of high-velocity impactor when compared with the conventional AA stacked BLG. To explore further deep computational insights of the ballistic performance of tBLG structures, a GPR based ML model is constructed with *RRA* (ranging from 0^o to 30^o due to symmetry) and V_i (ranging from 1 km/s to 6.5 km/s) as control variables. The proposed GPR based ML model accurately captures the variation of the ballistic performance measures of tBLG structures in a detailed high dimensional sample space including the effect of random system disorder following a large-scale data-driven probabilistic framework. The numerical results reveal that even a small degree of stochasticity in the form of random disorder in twist angle can result in significantly enhanced specific energy absorption capacity, which leads to the realization of prospective exploitation of such inevitable random disorders. A data-driven sensitivity analysis further unravels that the relative significance of *RRA* is lower compared to initial impact velocity. In the context of formation of the ML model, it is accurately identified that the physics of the system becomes significantly different beyond the impact velocity of 6.5 km/s due to the initiation of damage. It can be noted that such large-scale data-driven intricate details concerning high-velocity impact have been possible to capture primarily due to the augmented computational capabilities based on the GPR modelling.

The detailed mechanical behaviour of graphene and its multiple bilayer derivatives, as presented in this article including the effect of twisting and random disorder for their prospective exploitation, will accelerate the uptake of this nanostructure further as structural components in the development of a new class of composites with high strength-to-weight ratio to prevent high-velocity ballistic impact, which is common in defense and space applications.

Acknowledgment

KKG is grateful for the financial support from MoE, India during the research work. TM acknowledges the initiation grants received from IIT Kanpur.

References

Adhikari, S. and Chowdhury, R. (2012), "Zeptogram sensing from gigahertz vibration: Graphene based nanosensor", *Physica E*, **44**(7-8), 1528-1534. https://doi.org/10.1016/j.physe.2012.03.021.

Ávila, A.F., Neto, A.S. and Junior, H.N. (2011), "Hybrid nanocomposites for mid-range ballistic protection", *Int. J. Impact Eng.*, **38**(8-9), 669-676. https://doi.org/10.1016/j.ijimpeng.2011.03.002.

Azevedo, D.L., Bizao, R.A. and Galvao, D.S. (2018), "Molecular dynamics simulations of ballistic penetration of penta-graphene sheets", *MRS Adv.*, **3**(8-9), 433-437. https://doi.org/10.1557/adv.2018.61.

Bizao, R.A., Machado, L.D., de Sousa, J.M., Pugno, N.M. and Galvao, D.S. (2018), "Scale effects on the ballistic penetration of graphene sheets", *Sci. Rep.*, **8**(1), 1-8. https://doi.org/10.1038/s41598-018-25050-2.

Burn, M.J. and Popelier, P.L. (2020), "Creating Gaussian process regression models for molecular simulations using adaptive sampling", *J. Chem. Phys.*, **153(**5), 054111. https://doi.org/10.1063/5.0017887.

Chandra, Y., Adhikari, S., Mukherjee, S. and Mukhopadhyay, T. (2022), "Unfolding the mechanical properties of buckypaper composites: Nano-to macro-scale coupled atomistic-continuum simulations", *Eng. Comput.*, 1-31. https://doi.org/10.1007/s00366-021-01538-w.

Chandra, Y., Mukhopadhyay, T. and Adhikari, S. (2020), "Size-dependent dynamic characteristics of graphene based multi-layer nano hetero-structures", *Nanotechnology*, **31**(14), 145705. https://doi.org/10.1088/1361-6528/ab6231.

Cui, Y., Kundalwal, S.I. and Kumar, S. (2016), "Gas barrier performance of graphene/polymer nanocomposites", *Carbon*, **98**, 313-333. https://doi.org/10.1016/j.carbon.2015.11.018.

Deringer, V.L., Bartók, A.P., Bernstein, N., Wilkins, D.M., Ceriotti, M. and Csányi, G. (2021), "Gaussian process regression for materials and molecules", *Chem. Rev.*, **121**(16), 10073-10141. https://doi.org/10.1021/acs.chemrev.1c00022.

Dewapriya, M.A.N. and Meguid, S.A. (2019), "Comprehensive molecular dynamics studies of the ballistic resistance of multilayer graphene-polymer composite", *Comput. Mater. Sci.*, **170**, 09171. https://doi.org/10.1016/j.commatsci.2019.109171.

Dewapriya, M.A.N. and Miller, R.E. (2021), "Energy absorption mechanisms of nanoscopic multilayer structures under ballistic impact loading", *Comput. Mater. Sci.*, **195**, 110504. https://doi.org/10.1016/j.commatsci.2021.110504.

Farazin, A. and Mohammadimehr, M. (2020), "Nano research for investigating the effect of SWCNTs dimensions on the properties of the simulated nanocomposites: a molecular dynamics simulation", *Adv. Nano Res.*, **9**(2), 83-90. https://doi.org/10.12989/anr.2020.9.2.083.

Fazelzadeh, S.A. and Ghavanloo, E. (2014), "Nanoscale mass sensing based on vibration of single-layered graphene sheet in thermal environments", *Acta Mech. Sinica*, **30**(1), 84-91. https://doi.org/10.1007/s10409-013-0102-6.

Geim, A.K. and Novoselov, K.S. (2010), *The Rise of Graphene*, In *Nanoscience and Technology: A Collection of Reviews from Nature Journals*, World Scientific.

Gupta, K.K., Mukhopadhyay, T., Roy, A. and Dey, S. (2020), "Probing the compound effect of spatially varying intrinsic defects and doping on mechanical properties of hybrid graphene monolayers", *J. Mater. Sci. Technol.*, **50**, 44-58. https://doi.org/10.1016/j.jmst.2020.03.004.

Gupta, K.K., Mukhopadhyay, T., Roy, A., Roy, L. and Dey, S. (2021), "Sparse machine learning assisted deep computational insights on the mechanical properties of graphene with intrinsic defects and doping", *J. Phys. Chem. Solids*, **155**, 110111. https://doi.org/10.1016/j.jpcs.2021.110111.

Gupta, K.K., Roy, L. and Dey, S. (2022a), *Machine Learning-Based Molecular Dynamics Simulations of Monolayered Graphene*, In *Recent Advances in Computational and Experimental Mechanics*, Springer, Singapore.

Gupta, K.K., Mukhopadhyay, T., Roy, L. and Dey, S. (2022b), "Hybrid machine-learning-assisted quantification of the compound internal and external uncertainties of graphene: Towards inclusive analysis and design", *Mater. Adv.*, **3**, 1160-1181. https://doi.org/10.1039/D1MA00880C.

Haque, B.Z.G., Chowdhury, S.C. and Gillespie Jr, J.W. (2016), "Molecular simulations of stress wave propagation and perforation of graphene sheets under transverse impact", *Carbon*, **102**, 126-140. https://doi.org/10.1016/j.carbon.2016.02.033.

Hosseini-Hashemi, S., Sepahi-Boroujeni, A. and Sepahi-Boroujeni, S. (2018), "Analytical and molecular dynamics studies on the impact loading of single-layered graphene sheet by fullerene", *Appl. Surface Sci.*, **437**, 366-374. https://doi.org/10.1016/j.apsusc.2017.12.141.

Humphrey, W., Dalke, A. and Schulten, K. (1996), "VMD: Visual molecular dynamics", *J. Mol. Graph.*, **14**(1), 33-38. https://doi.org/10.1016/0263-7855(96)00018-5.

Kang, J.W., Kim, H.W., Kim, K.S. and Lee, J.H. (2013), "Molecular dynamics modeling and simulation of a graphene-based nanoelectromechanical resonator", *Curr. Appl. Phys.*, **13**(4), 789-794. https://doi.org/10.1016/j.cap.2012.12.007.

Kashyap, J., Yang, E.H. and Datta, D. (2020), "Computational study of the water-driven graphene wrinkle life-cycle towards applications in flexible electronics", *Sci. Rep.*, **10**(1), 1-15. https://doi.org/10.1038/s41598-020-68080-5.

Kwon, O.K., Lee, J.H., Park, J., Kim, K.S. and Kang, J.W. (2013), "Molecular dynamics simulation study on graphene-nanoribbon-resonators tuned by adjusting axial strain", *Current Applied Physics*, **13**(2), 360-365. https://doi.org/10.1016/j.cap.2012.08.009.

Kwon, S.R., Harris, J., Zhou, T., Loufakis, D., Boyd, J.G. and Lutkenhaus, J.L. (2017), "Mechanically strong graphene/aramid nanofiber composite electrodes for structural energy and power", *ACS Nano*, **11**(7), 6682-6690. https://doi.org/10.1021/acsnano.7b00790.

Lee, C., Wei, X., Kysar, J.W. and Hone, J. (2008), "Measurement of the elastic properties and intrinsic strength of monolayer graphene", *Science*, **321**(5887), 385-388. https://doi.org/10.1126/science.1157996.

Lee, J.H., Loya, P.E., Lou, J. and Thomas, E.L. (2014), "Dynamic mechanical behavior of multilayer graphene via supersonic projectile penetration", *Science*, **346**(6213), 1092-1096. https://doi.org/10.1126/science.1258544.

Li, Z., He, Q., Xu, X., Zhao, Y., Liu, X., Zhou, C., Ai, D., Xia, L. and Mai, L. (2018), "A 3D nitrogen-doped graphene/TiN nanowires composite as a strong polysulfide anchor for lithium–sulfur batteries with enhanced rate performance and high areal capacity", *Adv. Mater.*, **30**(45), 1804089. https://doi.org/10.1002/adma.201804089.

Lin, F., Xiang, Y. and Shen, H.S. (2017), "Temperature dependent mechanical properties of graphene reinforced polymer nanocomposites–a molecular dynamics simulation", *Compos. Part B Eng.*, **111**, 261-269. https://doi.org/10.1016/j.compositesb.2016.12.004.

Mahata, A., Mukhopadhyay, T. and Adhikari, S. (2016), "A polynomial chaos expansion based molecular dynamics study for probabilistic strength analysis of nano-twinned copper", *Mater. Res. Exp.*, **3**(3), 036501. https://doi.org/10.1088/2053-1591/3/3/036501.

MATLAB (2018), Version 18.10.0 (R2018a). https://www.mathworks.in

Mukhopadhyay, T., Mahata, A., Dey, S. and Adhikari, S. (2016), "Probabilistic analysis and design of HCP nanowires: An efficient surrogate based molecular dynamics simulation approach", *J. Mater. Sci. Technol.*, **32**(12), 1345-1351. https://doi.org/10.1016/j.jmst.2016.07.019.

Mukhopadhyay, T., Mahata, A., Adhikari, S. and Zaeem, M. (2017a), "Effective mechanical properties of multilayer nano-heterostructures", *Sci. Rep.*, **7**(1), 1-13. https://doi.org/10.1038/s41598-017-15664-3.

Mukhopadhyay, T., Mahata, A., Adhikari, S., and Zaeem, M. A. (2017b), "Effective elastic properties of two dimensional multiplanar hexagonal nanostructures", *2D Mater.*, **4**(2), 025006. https://doi.org/10.1088/2053-1583/aa551c.

Mukhopadhyay, T., Mahata, A., Naskar, S. and Adhikari, S. (2020), "Probing the effective Young's modulus of 'magic angle'inspired multi-functional twisted nano-heterostructures", *Adv. Theory Simul.*, **3**(10), 2000129. https://doi.org/10.1002/adts.202000129.

Naskar, S., Shingare, K.B., Mondal, S. and Mukhopadhyay, T. (2022), "Flexoelectricity and surface effects on coupled electromechanical responses of graphene reinforced functionally graded nanocomposites: A unified size-dependent semi-analytical framework", *Mech. Syst. Signal Pr.*, **169**, 108757. https://doi.org/10.1016/j.ymssp.2021.108757.

Noori, H., Mortazavi, B., Keshtkari, L., Zhuang, X. and Rabczuk, T. (2021), "Nanopore creation in MoS_2 and graphene monolayers by nanoparticles impact: A reactive molecular dynamics study", *Appl. Phys. A*, **127**(7), 1-13. https://doi.org/10.1007/s00339-021-04693-5.

O'Connor, T.C., Andzelm, J. and Robbins, M.O. (2015), "AIREBO-M: A reactive model for hydrocarbons at extreme pressures", *J. Chem. Phys.*, **142**(2), 024903 https://doi.org/10.1063/1.4905549.

O'Masta, M.R., Russell, B.P. and Deshpande, V.S. (2017), "An exploration of the ballistic resistance of multilayer graphene polymer composites", *Extreme Mech. Lett.*, **11**, 49-58. https://doi.org/10.1016/j.eml.2016.12.001.

Peng, Q., Peng, S. and Cao, Q. (2021), "Ultrahigh ballistic resistance of twisted bilayer graphene", *Crystals*, **11**(2), 206. https://doi.org/10.3390/cryst11020206.

Plimpton, S. (1995), "Fast parallel algorithms for short-range molecular dynamics", *J. Comput. Phys.*, **117**(1), 1-19. https://doi.org/10.1006/jcph.1995.1039.

Qiu, Y., Zhang, Y., Ademiloye, A.S. and Wu, Z. (2020), "Molecular dynamics simulations of single-layer and rotated double-layer graphene sheets under a high velocity impact by fullerene", *Comput. Mater. Sci.*, **182**, 109798. https://doi.org/10.1016/j.commatsci.2020.109798.

Roy, A., Gupta, K.K., Naskar, S., Mukhopadhyay, T. and Dey, S. (2021), "Compound influence of topological defects and heteroatomic inclusions on the mechanical properties of SWCNTs", *Mater. Today Commun.*, **26**, 102021. https://doi.org/10.1016/j.mtcomm.2021.102021.

Sha'bani, F. and Rash-Ahmadi, S. (2021), "Molecular dynamics investigation of pull-in instability in graphene sheet under electrostatic and van der Waals forces", *Adv. Nano Res.*, **11**(2), 173-181. https://doi.org/10.12989/anr.2021.11.2.173.

Shahini, E., Rangriz, F., Karimi Taheri, A. and Abdi-Jalebi, M. (2021), "Optimizing structural and mechanical properties of coiled carbon nanotubes with NSGA-II and reactive molecular dynamics simulation", *J. Phys. Chem. C*, **125**(11), 6237-6248. https://doi.org/10.1021/acs.jpcc.1c00073.

Sharma, V., Mitlin, D. and Datta, D. (2021), "Understanding the Strength of the Selenium–Graphene Interfaces for Energy Storage Systems", *Langmuir*, **37**(6), 2029-2039. https://doi.org/10.1021/acs.langmuir.0c02893.

Shingare, K.B. and Kundalwal, S.I. (2019), "Static and dynamic response of graphene nanocomposite plates with flexoelectric effect", *Mech. Mater.*, **134**, 69-84. https://doi.org/10.1016/j.mechmat.2019.04.006.

Shoaib, H., Peng, Q. and Alsayoud, AQ. (2021), "Atomic insights into fracture characteristics of twisted tri-layer graphene", *Crystals*, **11**(10),1202. https://doi.org/10.3390/cryst11101202.

Song, W.L., Guan, X.T., Fan, L.Z., Zhao, Y.B., Cao, W.Q., Wang, C.Y. and Cao, M.S. (2016), "Strong and thermostable polymeric graphene/silica textile for lightweight practical microwave absorption composites", *Carbon*, **100**, 109-117. https://doi.org/10.1016/j.carbon.2016.01.002.

Stankovich, S., Dikin, D.A., Dommett, G.H., Kohlhaas, K.M., Zimney, E.J., Stach, E.A., Piner, R.D., Nguyen, S.T. and Ruoff, R.S. (2006), "Graphene-based composite materials", *Nature*, **442**(7100), 282-286. https://doi.org/10.1038/nature04969

Stukowski, A. (2009), "Visualization and analysis of atomistic simulation data with OVITO–the open visualization tool", *Model. Simul. Mater. Sc.*, **18**(1), 015012. https://doi.org/10.1088/0965-0393/18/1/015012.

Sunnardianto, G.K., Bokas, G., Hussein, A., Walters, C., Moultos, O.A. and Dey, P. (2021), "Efficient hydrogen storage in defective graphene and its mechanical stability: A combined density functional theory and molecular dynamics simulation study", *Int. J. Hydrogen Energ.*, **46**(7), 5485-5494. https://doi.org/10.1016/j.ijhydene.2020.11.068.

Tersoff, J. (1988), "New empirical approach for the structure and energy of covalent systems", *Phys. Rev. B*, **37**(12), 6991. https://doi.org/10.1103/PhysRevB.37.6991.

Tian, W., Li, W., Liu, X. and Wang, Y. (2017), "Molecular dynamics study on the resonance properties of a nano resonator based on a graphene sheet with two types of vacancy defects", *Appl. Sci.*, **7**(1), 79. https://doi.org/10.3390/app7010079.

Tian, H., Zhang, B. and Li, Q.M. (2019), "Ballistic response of hexagonal boron nitride monolayer under impact of a nano-projectile", *Mech. Mater.*, **133**, 1-12. https://doi.org/10.1016/j.mechmat.2019.03.003.

Trinh, M.C. and Mukhopadhyay, T. (2021), "Semi-analytical atomic-level uncertainty quantification for the elastic properties of 2D materials", *Mater. Today Nano*, **15**, 100126. https://doi.org/10.1016/j.mtnano.2021.100126.

Wong, K.L., Chuan, M.W., Chong, W.K., Alias, N.E., Hamzah, A., Lim, C.S. and Tan, M.L.P. (2019), "Modeling of low-dimensional pristine and vacancy incorporated graphene nanoribbons using tight binding model and their electronic structures", *Adv. Nano Res.*, **7**(3), 209-221. https://doi.org/10.12989/anr.2019.7.3.209.

Xia, K., Zhan, H., Hu, D.A. and Gu, Y. (2016), "Failure mechanism of monolayer graphene under hypervelocity impact of spherical projectile", *Scientific Rep.*, **6**(1), 1-10. https://doi.org/10.1038/srep33139.

Yang, X. and Zhang, B. (2021), "Twisted bilayer graphene/h-BN under impact of a nano-projectile", *Appl. Surf. Sci.*, **538**, 148030. https://doi.org/10.1016/j.apsusc.2020.148030.

Yin, H., Sun, Z., Wang, Z., Tang, D., Pang, C.H., Yu, X., Barnard, A.S., Zhao, H. and Yin, Z. (2021), "The data-intensive scientific revolution occurring where two-dimensional materials meet machine learning", *Cell Rep. Phys. Sci.*, 100482. https://doi.org/10.1016/j.xcrp.2021.100482.

Yoon, K., Ostadhossein, A. and Van Duin, A.C. (2016), "Atomistic-scale simulations of the chemomechanicalbehavior of graphene under nanoprojectile impact", *Carbon*, **99**, 58-64. https://doi.org/10.1016/j.carbon.2015.11.052.

Zhang, X., Chen, Z., Chen, H. and Xu, L. (2021), "Comparative studies of thermal conductivity for bilayer graphene with different potential functions in molecular dynamic simulations", *Results Phys.*, **22**, 103894.

https://doi.org/10.1016/j.rinp.2021.103894.
Zheng, S., Cao, Q., Liu, S. and Peng, Q. (2019), "Atomic structure and mechanical properties of twisted bilayer graphene", *J. Compos. Sci.*, **3**(1), 2. https://doi.org/10.3390/jcs3010002.
Goswami, A.D., Mishra, M.K., Patra, D. (2016), "Adapting pattern recognition approach for uncertainty assessment in the geologic resource estimation for Indian iron ore mines", *Proceedings of the 2016 International Conference on Signal Processing, Communication, Power and Embedded System*, Paralakhemundi, India, June.
Quinonero-Candela, J., Rasmussen, C.E. (2005), "A unifying view of sparse approximate Gaussian process regression", *J. Mach. Learn. Res.*, **6**, 1939-59.

SR

Appendix

A1. Post-processing of the ballistic impact simulations

The residual velocity of an impactor is determined by observing the time history of the varying velocity of the impactor as depicted in Fig. S1(A). The double peaks visible in the Fig. S1(A) for the impact velocities less than 5 km/s, indicate rebound of the impactor, wherein the later increase in the residual velocity is due to the contribution of graphene structure in the rebound velocity of impactor. On the contrary, the later increase in the residual velocity is missing in the case of 5 km/s (or higher if calculated), which indicates the complete penetration of the graphene sheet. To evaluate the specific penetration energy of an impacted structure, Eq. (4) in the manuscript is used. The estimation of initial kinetic energy (KE_i) and residual kinetic energy (KE_r) of an impactor is carried out by observing the time history of the variation in kinetic energy as shown in Fig. S1(B).

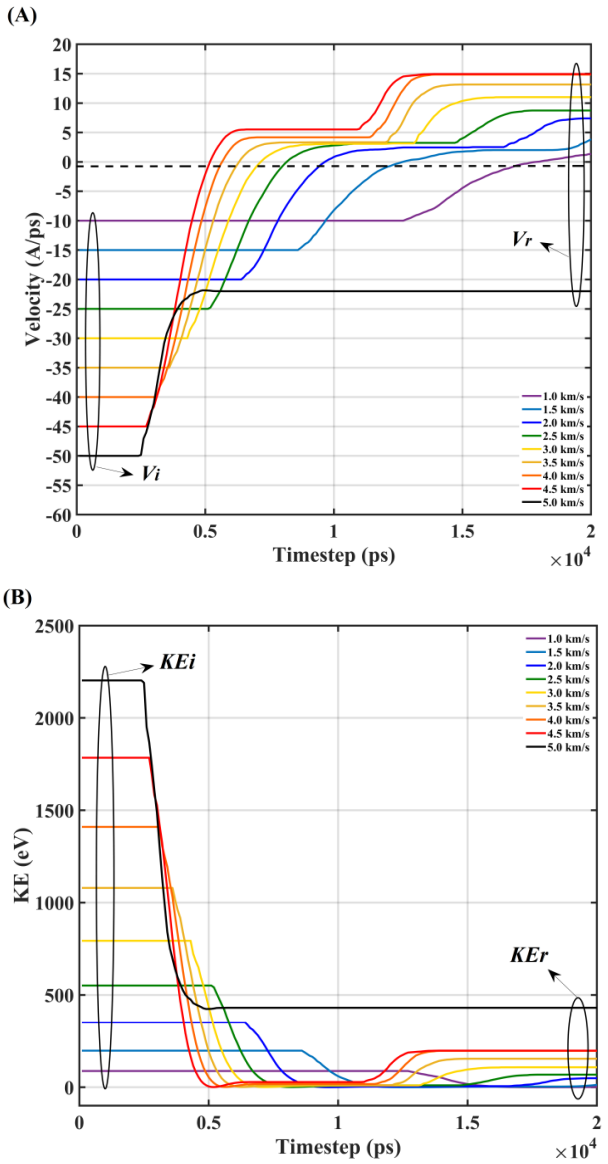

Fig. S1 Time history of (A) velocity of the impactor (B) kinetic energy of the impactor

A2. Gaussian process regression

Gaussian process regression (GPR) based ML models are nonparametric kernel-based probabilistic models (Goswami *et al.* 2016, Quinonero-Candela and Rasmussen 2005). Consider the training set $\{(x_i, y);\ i = 1, 2, \ldots n\}$, where $x_i \in R^d$ and $y_i \in R$, drawn from an unknown distribution. A GPR model addresses the question of predicting the value of a response variable y_{new}, given the new input vector x_{new}, and the training data. A linear regression model is of the form

$$y = x^T\beta + \varepsilon \tag{A1}$$

where $\varepsilon \approx N(0, \sigma^2)$. The error variance σ^2 and the coefficients β are estimated from the data. A GPR model explains the response by introducing latent variables, $f(x_i)$, $i = 1, 2, \ldots n$ from a Gaussian process (GP), and explicit basis functions, h. The covariance function of the latent variables captures the smoothness of the response and basis functions project the inputs x into a p-dimensional feature space.

A GP is a set of random variables, such that any finite number of them has a joint Gaussian distribution. If $\{f(x), x \in R^d\}$is a GP, then given n observations $x_1, x_2, \ldots, x_n$, the joint distribution of the random variables$f(x_1)$, $f(x_2), \ldots, f(x_n)$ is Gaussian. A GP is defined by its mean function $m(x)$ and covariance function, $k(x, x')$. That is, if $\{f(x), x \in R^d\}$ is a Gaussian process, then $E(f(x)) = m(x)$, and $Cov[f(x), f(x')] = E[\{f(x) - m(x)\}\{f(x') - m(x')\}] = k(x, x')$.

Now consider the following model.

$$\mathrm{h(x)} = \mathrm{T}\beta + \mathrm{f(x)} \tag{A2}$$

where $f(x_n) \sim GP(0, k(x, x'))$, that is $f(x)$ are from a zero mean GP with covariance function, $k(x, x')$. $h(x)$ are a set of basis functions that transform the original feature vector x in R_d into a new feature vector $h(x)$ in R^p. β is a p-by-1 vector of basis function coefficients. This model represents a GPR model. An instance of response y can be modeled as

$$p(y_i|f(x_i), x_i) \approx N(y_i|h(x_i)^T\beta + f(x_i), \sigma^2) \tag{A3}$$

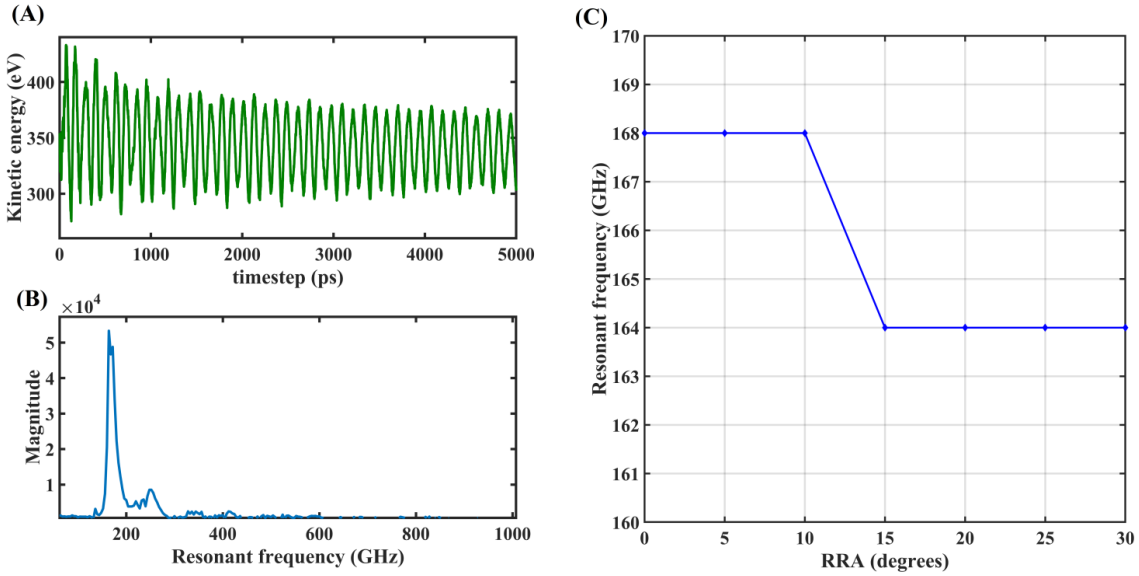

Fig. S2 (A) Time-domain signal of the post-impact kinetic energy of SLGS under free vibration (B) FFT of time-domain kinetic energy signal depicted in figure S2(A) (C) The variation in the resonant frequency of tBLG structures as a function of RRA. Each graphene nanostructure considered here has 200Å x 200Å size and is enforced with the CCCC boundary condition.

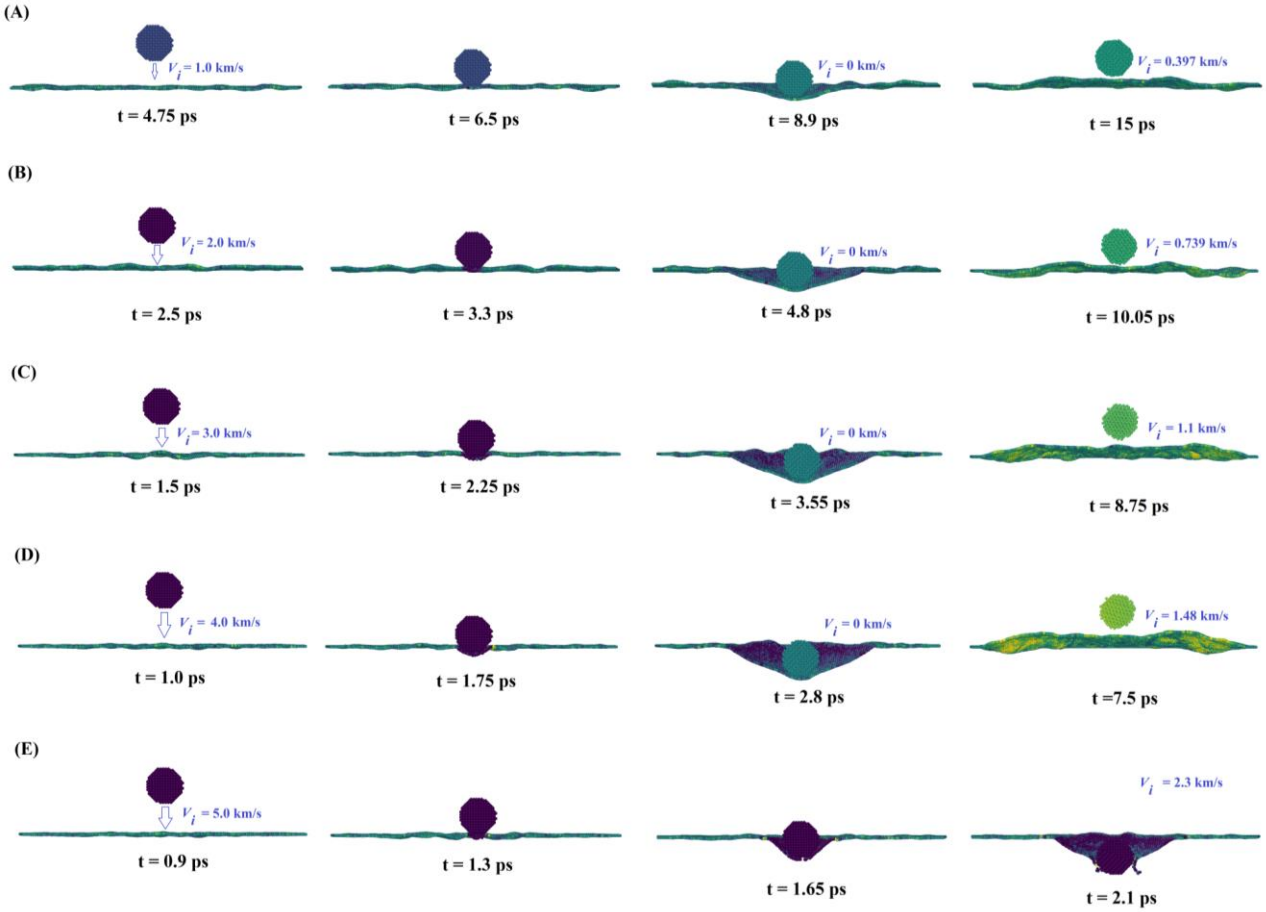

Fig. S3 Atomistic trajectory of high velocity impact of spherical diamond projectile (D_i = 25 Å) on the SLGS (size: 200 Å x 200 Å) (A) at impact velocity V_i = 1.0 km/s (B) at impact velocity V_i = 2.0 km/s (C) at impact velocity V_i = 3.0 km/s (D) at impact velocity V_i = 4.0 km/s (E) at impact velocity V_i = 5.0 km/s. The value of '*t*' provided at the bottom of each frame denotes the time in picoseconds

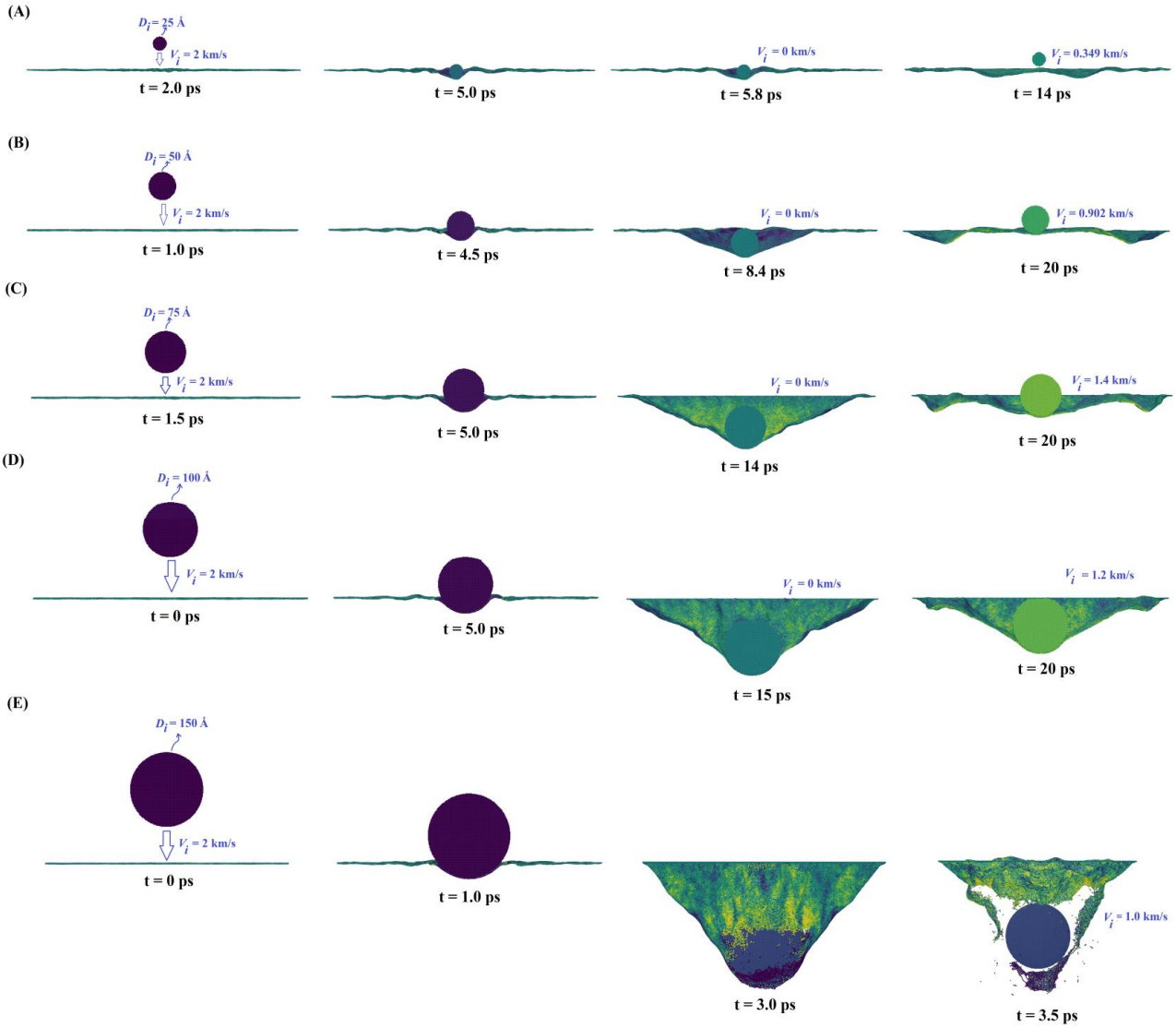

Fig. S4 Atomistic trajectory of high velocity impact (V_i = 2.0 km/s) on the SLGS (size: 500 Å x 500 Å) by spherical diamond projectile of (A) diameter, D_i = 25 Å (B) diameter, D_i = 50 Å (C) diameter, D_i = 75 Å (D) diameter, D_i = 100 Å (E) diameter, D_i = 150 Å. The value of '*t*' provided at the bottom of each frame denotes the time in picoseconds

Hence, a GPR model is a probabilistic model. There is a latent variable $f(x_i)$ introduced for each observation x_i, which makes the GPR model nonparametric. In vector form, this model is equivalent to

$$p(y|f,X) \approx N(y|H\beta + f, \sigma^2) \tag{A4}$$

where

$$X = \begin{pmatrix} x_1^T \\ x_2^T \\ \vdots \\ x_n^T \end{pmatrix}, y = \begin{pmatrix} y_1 \\ y_2 \\ \vdots \\ y_n \end{pmatrix}, H = \begin{pmatrix} h(x_1^T) \\ h(x_2^T) \\ \vdots \\ h(x_n^T) \end{pmatrix}, f = \begin{pmatrix} f(x_1) \\ f(x_2) \\ \vdots \\ f(x_n) \end{pmatrix} \tag{A5}$$

The joint distribution of latent variables $f(x_1)$, $f(x_2)$, … $f(x_n)$ in the GPR model is as follows

$$P(f|X) \approx N(f|0, K(X,X)) \tag{A6}$$